Gondwana Research 111 (2022) 223–248

Contents lists available at ScienceDirect

Gondwana Research

journal homepage: www.elsevier.com/locate/gr

The lower oceanic crust at ultraslow-spreading Southwest Indian Ridge: The inside story

Archisman Dhar [a], Biswajit Ghosh [a,*], Debaditya Bandyopadhyay [a,b], Tomoaki Morishita [c], Akihiro Tamura [c], Lydéric France [d], Du K. Nguyen [e], Marine Boulanger [d], Manojit Koley [a], Sankhadeep Roy [a], Soumi Chattopadhaya [a]

[a] Department of Geology, University of Calcutta, 35 Ballygunge Circular Road, Kolkata 700019, India
[b] Earthquake Research Institute, The University of Tokyo, Tokyo 113-0032, Japan
[c] School of Natural System, College of Science and Engineering, Kanazawa University, Japan
[d] Université de Lorraine, CNRS, CRPG, Nancy, France
[e] Faculty of Geosciences and Geoengineering, Hanoi University of Mining and Geology, Hanoi 100000, Vietnam

ARTICLE INFO

Article history:
Received 11 September 2021
Revised 5 July 2022
Accepted 17 August 2022
Available online 24 August 2022
Handling Editor: Z. Zhang

Keywords:
IODP 360
Atlantis Bank
Lower crust
Gabbro
Assimilation and fractional crystallization

ABSTRACT

Owing to the lack of persistent magma chamber and the complex interplay between magmatism and tectonism at slow- to ultraslow-spreading ridges, the likeliness of fractional crystallization being the predominant process of evolution of crustal magmas is weak. Here, we report a detailed petro-geochemical investigation from the lower crustal gabbroic rocks recovered from Hole U1473A in Atlantis Bank oceanic core complex, Southwest Indian Ridge that may potentially provide new insights on the dynamic accretion process at ultraslow-spreading ridge. Sampling the entire lithological spectrum encompassing a single geochemical cycle in this study permit us to probe the underlying magmatic processes in ultraslow-spreading lower crust. Grain-size variation is ubiquitously recorded in the gabbroic lithologies of Hole U1473A, where fine-grained intervals represent relatively evolved chemistry than the coarser domains. This suggests that, they were crystallized from a common genetic melt during different degrees of evolution. The forward geochemical modelling approach have not only affirmed the long-established theory of assimilation (of early mushes' crystals)-fractional crystallization to be the key mechanism in lower crust formation, but also provided explanation for the restricted whole rock geochemical cluster observed throughout all the rock types. We demonstrate for the first time the relationship between the progressive modal mineralogical evolution with respect to the different assimilation/fractionation ratios (r). The observed trend has been successfully replicated for the experiments with high r values = 0.8–0.9, previously predicted from this region. Integrating all results, our study supports the model of lower crustal formation via reactive porous flow of the squeezed-out melt percolating throughout the cumulate pile and segregated into different horizons.
© 2022 International Association for Gondwana Research. Published by Elsevier B.V. All rights reserved.

1. Introduction

The accretion of new crust at mid-ocean ridges and its destruction at subduction zones is the foundation process of plate tectonic cycle. Mid-ocean ridges are by far the commonest plate boundary class (~67,000 km long) accommodating the most abundant magmatic process for transferring heat and mass from the Earth's interior to the outer envelope. The extent of decompressional melting of adiabatically upwelling mantle, depending on factors like potential temperature, composition and efficacy of the system for melt extraction from areas undergoing melting greatly controls the spreading rate, morphology and architecture of the ridges. Unlike the fast-spreading ridges where magma flux is high, leading to systematic injection of melt into the lower crust (White & Klein, 2014; Dick et al., 2017), the slow- and ultraslow-spreading ridges dominantly are marked by lack of any steady-state axial magma chamber (Detrick et al., 1987; Van Ark et al., 2007). However, findings of Jian et al. (2017a,b) have shown the ponding of magma at the top of axial magma chamber beneath ultraslow spreading Southwest Indian Ridge (SWIR).

Plate spreading in magmatically starved slow- and ultraslow-spreading ridges is largely accommodated in the lower crust by tectonic extension due to faulting (Cann et al., 1997; Cannat

* Corresponding author.
E-mail address: bghosh_geol@hotmail.com (B. Ghosh).

https://doi.org/10.1016/j.gr.2022.08.008
1342-937X/© 2022 International Association for Gondwana Research. Published by Elsevier B.V. All rights reserved.

et al., 2006; Sauter et al., 2013) and to certain extent by ductile deformation (Mutter and Karson, 1992). Uplifted footwalls of these low-angle, large-offset detachment faults represent a segment of lower crust and mantle rocks exhumed over time by asymmetric spreading, manifesting finally into an oceanic core complex (OCC) or megamullion (Cannat, 1993; Cann et al., 1997; MacLeod et al., 2009). OCCs are typically developed when the magmatism is suppressed over a time-scale of 10^6 yr, and ridge-axis is in the length scale of 20–30 km (Buck et al., 2005; Tucholke et al., 2008; MacLeod et al., 2009). Weakening of ridge flank faults by secondary hydrous minerals formation also facilitates the process (MacLeod et al., 2009). Nevertheless, the magma supply along long-lived detachment faults may vary over a range, producing diverse lower crustal architecture (Tucholke et al., 2008; Olive et al., 2010). Lower crust in the high magma-supply end-member OCC is distinctly heterogeneous and compositionally anisotropic compared to relatively homogeneous crust with no large-scale variation formed at low magma-supply OCC. The OCC segments are long been considered coveted sites of petro-geochemical investigations because, lower crust that could be accessed here preserves physico-chemical signatures of melt transport from mantle to the crust. Studies carried out on OCC segments in last five decades have yielded valuable insights on the ridge systematics at slow- to ultraslow-spreading centres (Dick et al., 2000, 2017, 2019a, 2019b; Gao et al., 2007; Niu et al., 2002; Godard et al., 2009; Lissenberg and Dick, 2008; Lissenberg and MacLeod, 2016; Sanfilippo et al., 2015, 2019; Boulanger et al., 2020, 2021; Ferrando et al., 2021a, 2021b). The magmatic system in the lower oceanic crust in these environments is believed to be dominantly crystal mush with episodic supply of magma in the absence of any persistent magma body (Nisbet and Fowler, 1978; Sinton and Detrick, 1992; Natland and Dick, 2001; Sinha et al., 1997, 1998; Magde et al., 2000; Singh et al., 2006; Canales et al., 2017; Jian et al., 2017a). However, Perfit and Chadwick (1998) have suggested that although infrequent, individual eruptions at slow-spreading ridges are generally larger than at fast-spreading centres. Complex zoning pattern, reaction textures, mineral modes and compositions recorded from lower crustal rocks indicate that simple fractional crystallization is not the only process shaping the lower oceanic crust. Detailed petrological and geochemical studies highlight that, the reactive porous flow associated with migration of melt throughout the crustal section plays an important role in modifying the composition of the lower crust (Meyer et al., 1989; Coogan et al., 2000; Dick et al., 2002; Ridley et al., 2006; Gao et al., 2007; Lissenberg and MacLeod, 2016; Sanfilippo et al., 2015; Boulanger et al., 2020; Ferrando et al., 2021a).The extent of melt-rock reaction in OCC gabbroic rocks at slow- and ultraslow-spreading ridges is largely controlled by the complex interplay between magma injections and tectonic stresses (Brunelli et al., 2020; Dick et al., 1991a; Natland and Dick, 2001; Sanfilippo et al., 2019; Boulanger et al., 2020; 2021; Tribuzio et al., 2020; Ferrando et al., 2021b).

Drilling through Atlantis Bank, an OCC at the south of segmented SWIR and sampling Hole U1473A, the only borehole drilled during International Ocean Discovery Program (IODP) expedition 360 provide a window to understand the lower oceanic crust forming processes at ultraslow-spreading ridges. Most of the rocks recovered from U1473A are olivine-gabbros, intermingled with highly evolved oxide-gabbros. On the contrary a wider range of rocks have been recovered from the 1.4 km deep Hole U1309D at Atlantis massif OCC along the Mid-Atlantic Ridge (MAR). Troctolite along with gabbro (sensu stricto; olivine < 5 vol%) and minor amount of evolved gabbros (oxide > 2 vol%) constitute Hole U1309D (Blackman, 2006; Blackman and Collins, 2010). Absence of primitive cumulates like troctolite in Hole U1473A indicates that, its parental melt is likely not very close to a primary magmatic melt (Dick et al., 2000; MacLeod et al., 2017). An ubiquitous feature of the Hole U1473A lithologies is the presence of primary igneous layering defined mainly by sharp grain-size variation with/without modal variation throughout the core, conspicuous at certain depth intervals (Dick et al., 2017). Multi-stage permeable melt migration involving an early-stage compaction-driven oxide-undersaturated melt transport at lower level and a late-stage deformation-triggered oxide-saturated melt transport at upper level through Atlantis Bank lower crust has recently been invoked (Zhang et al., 2020). Crystallization of melts modified by reactive melt migration has been linked with the formation of fine-grained intervals (Ferrando et al., 2021a; Boulanger et al., 2021). Of late, using corrections in mineral-melt partition coefficients both for temperature and composition, applicable for an evolving melt undergoing assimilation-fractional crystallization (AFC) process Sanfilippo et al. (2020) propose reactive porous flow of residual interstitial melts through primitive olivine gabbro crystal mushes as an important mechanism in the evolution of lower crustal rocks.

Here, in this contribution we have tested the role of AFC process to reproduce the compositional (bulk rock and mineral trace element) and modal variability of lithologies from the lower part of Hole U1473A which is the less deformed interval (Dick et al., 2017) and where grain-size variation is more pronounced. We have performed AFC modelling, using alpha-MELTS (Smith and Asimow, 2005; Ghiorso and Sack, 1995) at different assimilation/fractionation ratios (r) over a range of temperature and integrated the result with mineral chemical and bulk rock analytical data. The strength of this study is that it is not focused to a particular rock type, instead it encompasses an array of gabbroic lithotypes, ranging from relatively primitive olivine gabbro to evolved oxide-gabbro; also, it relies on detailed whole rock chemistry, phase composition and modal compositions of the entire lithological range, thus depicting the holistic inside story. Further, this study could eliminate possibilities of any sampling bias since sample selection (shipboard) was done across all visible layer interfaces of the interlayered gabbroic rocks of Hole U1473A.

2. Geological framework and sampling from U1473A

Atlantis Bank (32°43′S, 57°17′E) is the shallowest part of the SWIR, located at 95 km south of the ridge segment AN1 on the eastern flank of Atlantis II transform fault (Fig. 1). The bank was uplifted to as shallow as 700 m below sea level (mbsl) from the bottom of the transform wall (Dick et al., 1991a; Baines et al., 2003; Hosford et al., 2003; Dick et al., 2017). The ~25 km^2 wave-cut terrace exposes mostly submerged gabbros from deeper part of the oceanic crust with various types of sediments around; presence of detachment fault footwall and damage zone (occurrences of cataclasized gabbro mylonites) have been also documented below Atlantis Bank (Dick et al., 1991a; Dick et al., 2017). Several lines of geophysical, petrological and geochronological evidences postulated Atlantis Bank as an 11–13 My old elevated OCC, emplaced by low-angle detachment fault into the rift mountains of SWIR (see Dick et al., 2017 and references therein).

Earlier seabed rockdrills have recovered deformed gabbros, diabase dikes, serpentinized peridotites and pillow-basalt breccias from different parts of the platform (MacLeod et al., 1998; Dick et al., 2019b). Hole U1473A was drilled at the summit of Atlantis Bank during IODP 360, 1–2 km away from two previous Ocean Drilling Program (ODP) holes: Hole 735B (drilled during ODP Leg 118 in 1987 and ODP Leg 176 in 1997) and Hole 1105A (drilled during ODP Leg 179 in 1998). Thus, the Atlantis Bank perhaps represents by far the most extensive lower crustal section recovered from slow-spreading ridges. A continuous process of magmatic

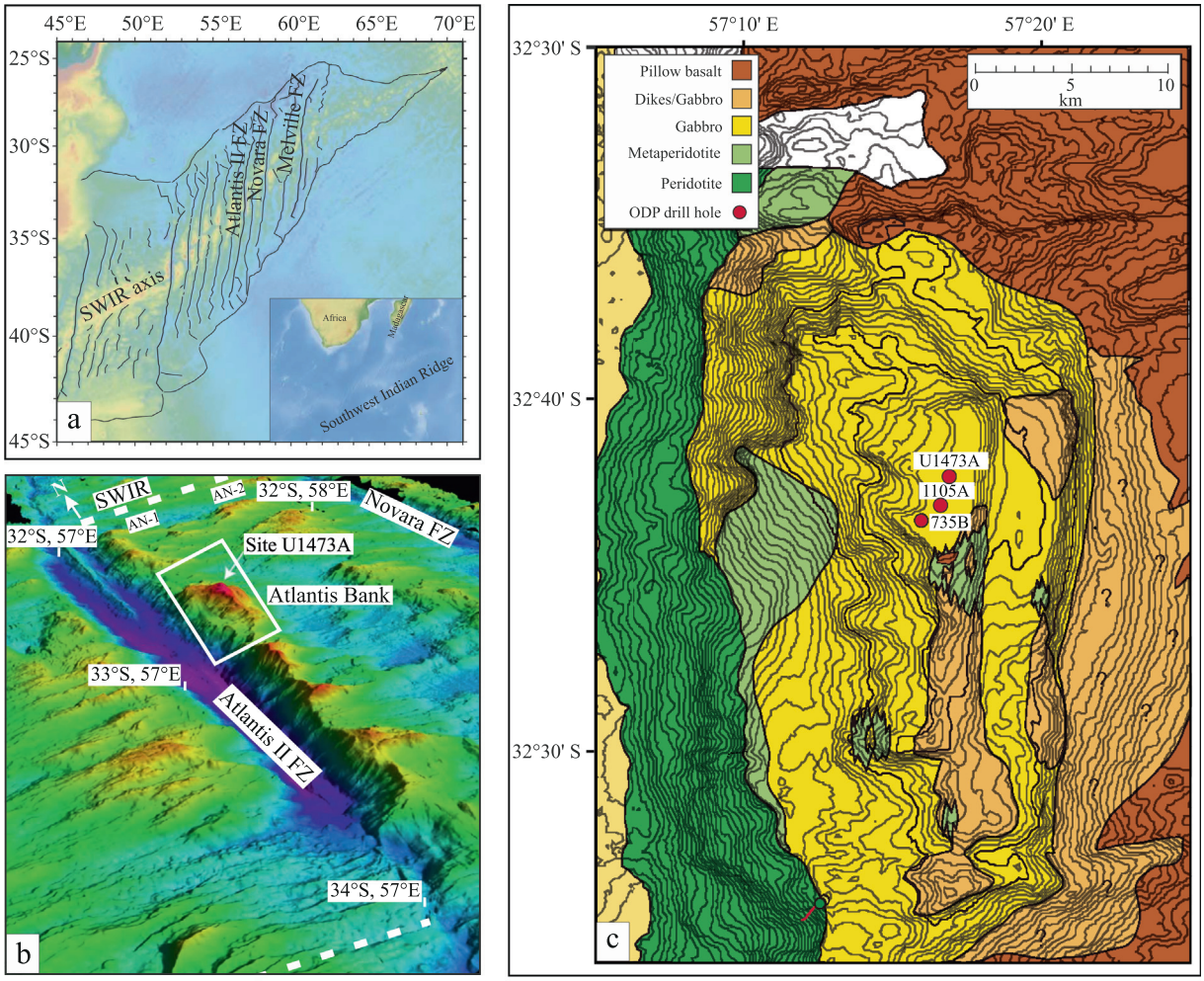

Fig. 1. a. Location map of Atlantis II Fracture Zone (modified from Meyzen et al., (2003), b. 3-D bathymetric map of Atlantis II Fracture Zone showing the location of Atlantis Bank Oceanic Core Complex (modified from MacLeod et al., 2017), c. geological map of Atlantis Bank Oceanic Core Complex showing the locations of ODP/IODP holes 735B, 1105A and U1473A (from Dick et al., 2017).

accretion along with detachment faulting operated throughout the lower oceanic crust can be envisaged while comparing Hole U1473A to Hole 735B and 1105A (Dick et al., 2017).

The gabbros recovered from both the above-mentioned ODP holes are dominantly adcumulates, consisting mostly of olivine gabbro, with subordinate amounts of oxide-gabbro, troctolite and leucocratic veins (Dick et al., 1991b, 2000; Pettigrew et al., 1999). The lithologies recovered from Hole U1473A include 76.5% olivine gabbro (olivine + plagioclase + clinopyroxene, none of which has modal abundance of <5%), 5.1% gabbro (plagioclase + clinopyrox ene > 95%, both the phases have modal abundance of > 10%), 9.5% disseminated-oxide gabbro (containing 1–2% Fe- Ti oxide), 3.7% oxide-bearing gabbro (2–5% Fe- Ti oxide), 3.7% oxide-gabbro (>5% Fe- Ti oxide) and 1.5% felsic veins. Small diabase dikes (not included in volume total) were also recovered (Dick et al., 2017; MacLeod et al., 2017). Based on the variation in mineral modes, grain size and textures, Hole U1473A gabbros were categorized into eight lithological units (Fig. 2), though other aspects such as the presence of igneous layering, felsic material, whole rock geochemistry, magnetic susceptibility were also taken into consideration during this categorization (Dick et al., 2017). Drilled crustal sections from different boreholes at Atlantis Bank are constructed by repeated cycles of intrusion, represented by gradual upward decrease of Mg#, Ca#, and Cr, Ni concentrations complemented by increase in Y content (Dick et al., 2017). Five such chemical cycles have been reported from Hole 735B (Dick et al., 2000) while three have been reported from Hole U1473A (Dick et al., 2017). An intriguing textural feature of these gabbro cumulates is the development of igneous layering defined by contrasting grain size, complemented by modal variation. Incipient layering is present in almost every unit. It can take the form of fine-grained patches or intervals with wavy contacts, or distinct layers with sharp, planar and sub-horizontal contacts. However, the layering is more pronounced in Unit II (91.29–175 m core composite depth below sea floor [CCSF]) and Unit VII – VIII (580–680 m CCSF) (Fig. 2) (Dick et al., 2017).

Here, in this study we have scrutinized 24 samples from depth 530–790 m CCSF corresponding to the bottom most geochemical cycle, which belong to Units VI, VII and VIII, (Dick et al., 2017). The densest occurrences of grain-size and modal contacts are found in the depth ranges of ~580–740 m and ~620–790 m CCSF respectively (Fig. 2). Also, degree of deformation across the entire range is quite low (Fig. 2). These factors led us to constrain the selection of samples into this part of the drilled core. Sampling was done across all visible layering (grain-size) interfaces irrespective of lithology to accommodate more than one layer in a single thin section. Therefore, each thin section consists of more than one layers, at least two, discriminated on the basis of grain size and/or complementary modal variation (Fig. 3). This excludes possibilities of any potential lithological bias during sampling. Detailed modal calculations of all the lithounits are presented in Supplemental Table S1. Olivine gabbros in general are less

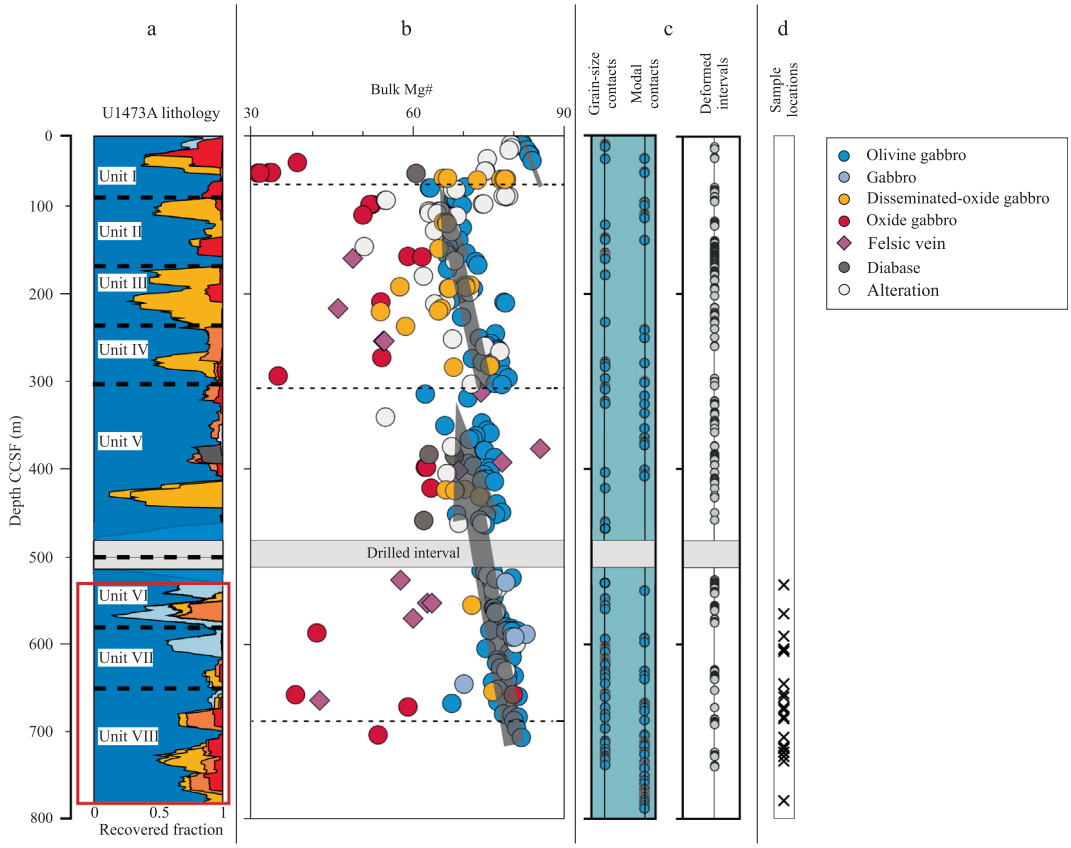

Fig. 2. Downhole variation of a. lithologic proportion (representing 20 m running average) [Dashed lines indicate unit boundaries. Studied area of the hole is marked by the rectangle], b. whole rock Mg# (100* cationic (Mg/Mg + Fe); all Fe considered as Fe^{2+}), c. contact types and deformation intervals of the recovered samples from Hole U1473A (modified from MacLeod et al., 2017). d. locations of the selected samples for this study.

deformed compared to oxide-bearing gabbros. Because of crystal-plastic deformation is severe at places, to understand the primary igneous features we have focused mostly on samples which are least deformed.

3. Petrography

3.1. Contact relationships between coarse- and fine-grained intervals

Grain-size variation is thoroughly recorded from the studied samples (Supplemental Table S1). Both fine- (<1mm) and medium-grained (1–3 mm) intervals within coarse-grained (>3 mm) horizons are common throughout the Hole U1473A. Two types of contacts have been delineated: (i) diffuse contacts-embayment of coarse-grained intervals within the finer ones (Fig. 3a), and (ii) relatively sharp boundaries between the coarser and finer horizons (Fig. 3b). Both the contacts however show suture and wavy margins on thin section scale. Coarsening of grain-size towards the interface is notable in Fig. 3a. Henceforth, we will be describing the grain-size layering in the studied samples in a nominal scale, coarser and finer, where the latter includes both fine- and medium-grained lithotypes in absolute scale.

3.2. Magmatic textures

3.2.1. Olivine gabbro and gabbro

Olivine gabbros predominantly consist of olivine, plagioclase and clinopyroxene with minor orthopyroxene, amphibole and Fe-Ti oxide. Modal abundances of the constituting phases vary appreciably, viz. ~49–68% plagioclase, ~17–43% clinopyroxene, and ~5–27% olivine. Gabbros on the other hand, are dominantly composed of plagioclase (~38–72%) and clinopyroxene (~24–62%) with or without little abundance of olivine (<5 %). At depth shallower than ~620 m, and 650–700 m CCSF there is a clear tendency of higher olivine and plagioclase and lower clinopyroxene in the coarser lithologies of olivine gabbro, whereas the finer lithologies below ~725 m CCSF contain more plagioclase than the coarser ones. (Supplemental Table S1).

Plagioclase grains are mostly subhedral to euhedral in shape, locally enclosed by large clinopyroxene (Fig. 4a, b) and olivine (Fig. 4c) oikocrysts. They show deformation twins at places (Fig. 4a, c). Clinopyroxenes commonly occur as granular phases, often forming large oikocrysts enclosing plagioclase (Fig. 4a, b) and olivine (Fig. 4d). Such ophitic and/or poikilitc nature of clinopyroxenes are ubiquitous in both coarser and finer units (Fig. 4a, b, d, e). Olivine grains are commonly anhedral in shape and occur as granular to intergranular phases locally (Fig. 4f) both in coarser and finer horizons. At places, small olivine grains are enclosed by plagioclase (Fig. 4a) and clinopyroxene (Fig. 4d) in poikilitic habit. Orthopyroxenes commonly occur as intercumulus phases, forming discontinuous bands between olivine and plagioclase boundaries (Fig. 4g, h). Amphiboles however record a variety of mode of occurrences in these gabbros (sensu lato). Brown amphiboles commonly occur as primary interstitial phase between the major minerals. Green or brownish green amphiboles are replacive in nature, mostly restricted at the boundaries of clinopyroxene.

3.2.2. Oxide-bearing lithologies

Oxide-bearing lithologies include disseminated-oxide gabbro (1–2 modal % oxide), oxide-bearing gabbro (2–5 modal % oxides) and oxide-gabbro (>5 modal % oxides) (Dick et al., 2017). They

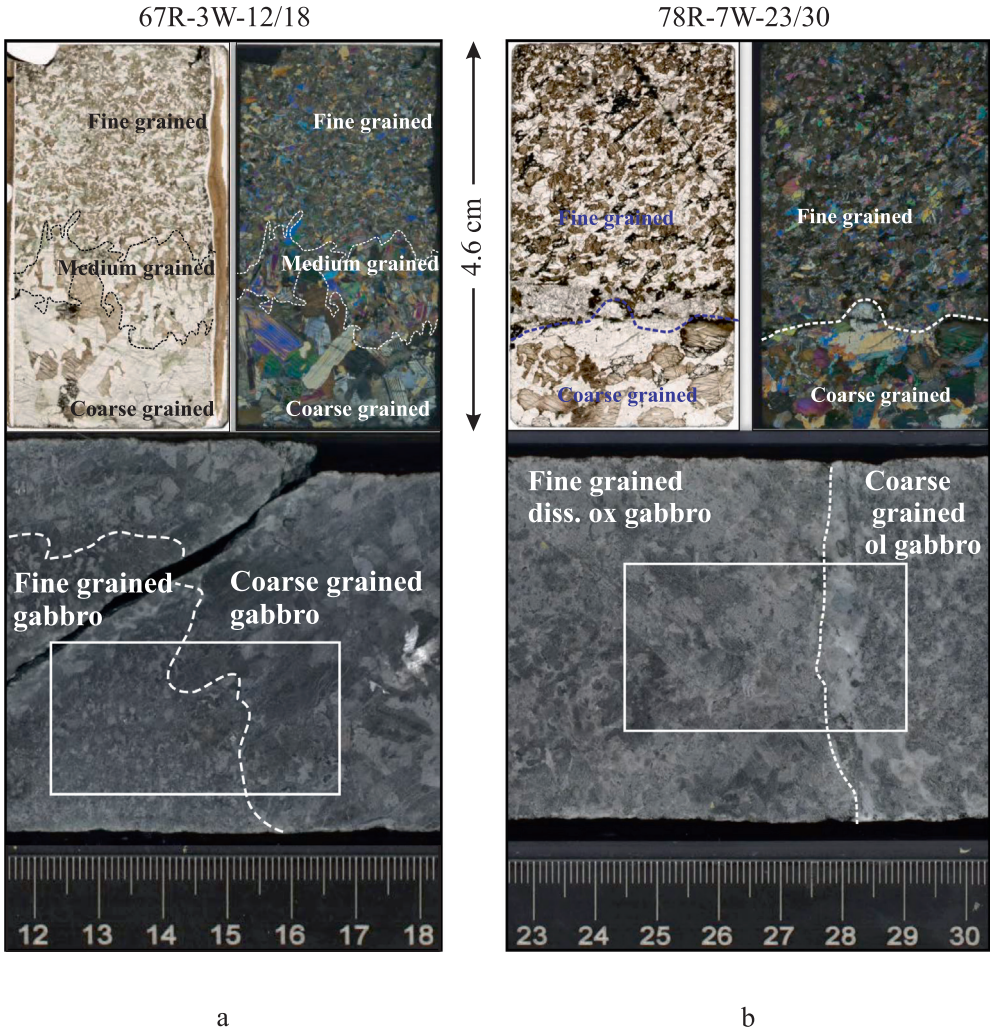

Fig. 3. Scanned thin sections of cores from different stratigraphic depths of U1473A showing grain-size variation. Different types of contacts are documented. a. diffused contact, b. sharp contact between two domains. White rectangles show the location of the this section made from this core.

are characterised by relatively higher proportions of orthopyroxene, amphibole and Fe-Ti oxide (Supplemental Table S1) compared to olivine gabbro and gabbro. Albeit having comparable modal abundances of constituting mineral phases in the coarser and finer lithologies, Fe-Ti oxide phases are distinctly higher in the former group. However, proportion of orthopyroxene is grossly similar in both coarser and finer horizons except one sample.

The major silicate phases, viz. plagioclase, clinopyroxene and olivine exhibit textures akin to olivine gabbros and gabbros. Small plagioclase chadacrysts are enclosed by clinopyroxene (Fig. 5a, b) and olivine oikocrysts (Fig. 5b). Also, small anhedral olivine grains are enclosed by large clinopyroxene oikocrysts at places (Fig. 5a). Irregular shaped Fe-Ti oxides often exhibit lobate boundary against embayed plagioclase, (Fig. 5c, d), clinopyroxene (Fig. 5c, e) and orthopyroxene (Fig. 5d). Olivine, plagioclase and amphibole may occur as islands in Fe-Ti oxides (Fig. 5d). Such occurrences of silicate phases with rounded contacts in oxides are common in both coarser and finer horizons (Fig. 5c-e). Occurrence of interstitial amphiboles in oxide-bearing rocks is more common than olivine gabbro and gabbro. Development of symplectitic intergrowth (Fe-Ti oxide + orthopyroxene symplectite) adjacent to olivine grains is recorded from certain horizons (Fig. 5f). Commonly, the symplectites occur where olivine is in contact, or nearly so, with magmatic magnetite, Ti-bearing magnetite or ilmenite crystals.

4. Analytical techniques

4.1. Mineral major and trace element chemistry

Major element analyses of pyroxenes, olivines, plagioclases and oxide minerals (ilmenite and magnetite) were carried out at Kanazawa University with an Electron Probe Micro Analyser (EPMA) (JEOL JXA-8800 Superprobe). Both natural and synthetic minerals were used for calibration. An accelerating voltage of 20 kV, a beam current of 20nA and a beam diameter of 3 μm were used while performing the analyses. Raw data correction was done using ZAF online correction program.

Trace element concentrations of clinopyroxenes were also analysed at Kanazawa University using a laser ablation (193 nm ArF excimer: MicroLas GeoLas Q-plus) inductively coupled plasma mass spectrometry (Agilent 7500S) (LA-ICP-MS). Each analysis was carried out by ablating 40–60 μm in diameter at 6 Hz with energy density of 8 J cm^{-1} per pulse. Signal integration times were 50 s for both gas background interval and ablation interval. The primary calibration standard for glass (NIST SRM 612) was selected from Pearce et al. (1997). In data reduction, ^{29}Si was used as internal standard for pyroxenes, based on SiO_2 contents determined by microprobe. This procedure is same as those mentioned in Longerich et al. (1996). The quality of analyses estimated from

Fig. 4. Photomicrographs of olivine gabbros in crossed polarised light. a. plagioclase chadacrysts enclosed by large clinopyroxene oikocryst, corroded olivine grain enclosed by plagioclase in coarser olivine gabbro, b. corroded boundary between olivine and plagioclase, c. small plagioclase grain enclosed by olivine oikocryst, large plagioclase grain showing deformation twins, d. inclusion of olivine grain in large clinopyroxene, e. inclusion of small plagioclase in clinopyroxene oikocryst from finer unit, f. olivine grains occurring as intergranular phase, g. orthopyroxene interstitial to plagioclase and olivine from coarser unit, h. orthopyroxene interstitial to plagioclase and olivine from finer unit. Abbreviations are as follows: Ol = olivine, Pl = plagioclase, Cpx = clinopyroxene, Opx = orthopyroxene.

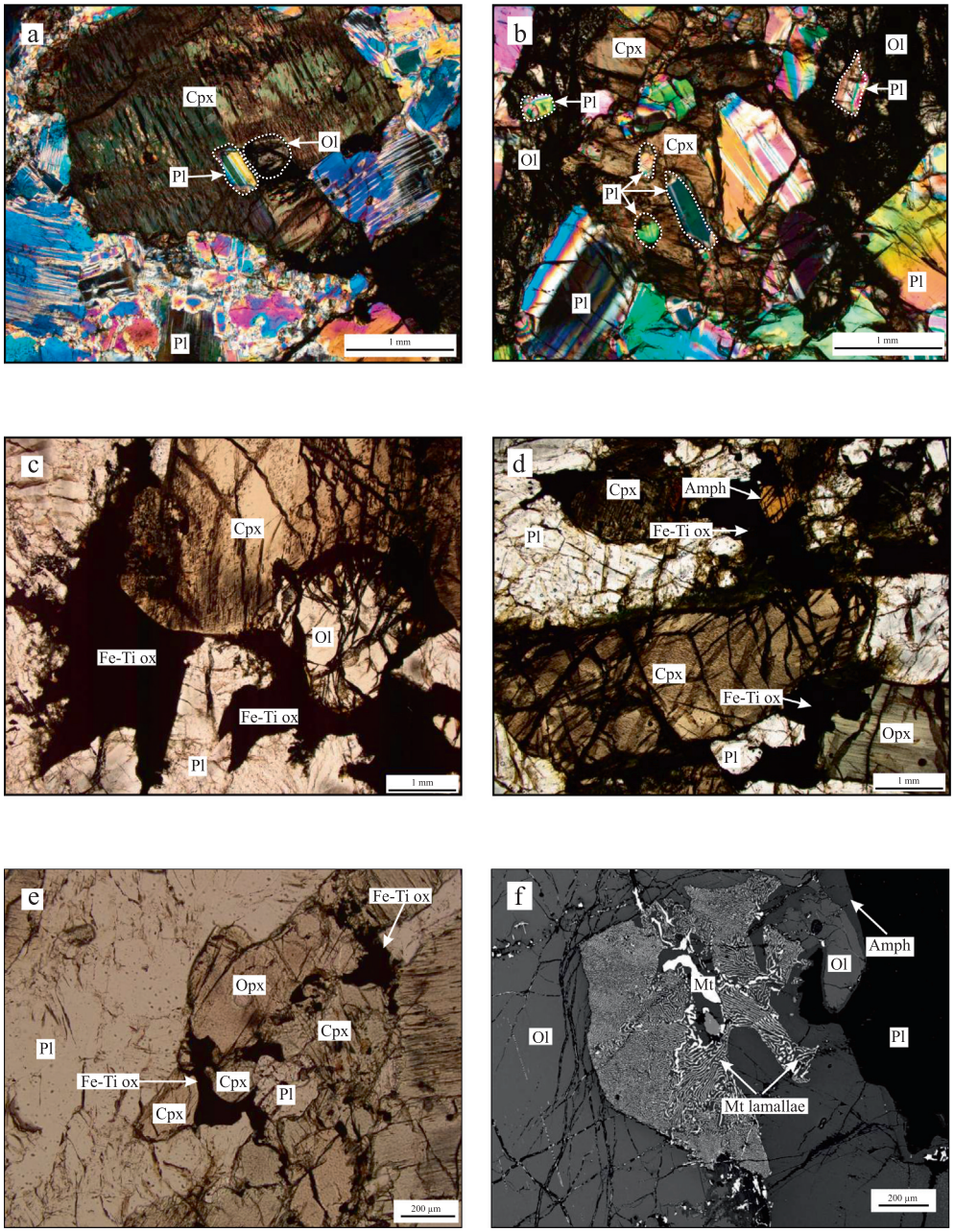

Fig. 5. Photographs of oxide bearing rocks in plane and crossed polarized light. a. small olivine and plagioclase grains enclosed by clinopyroxene oikocryst in coarser unit of oxide gabbro, b. inclusion of plagioclase in olivine in finer disseminated-oxide gabbro, c. corroded olivine, plagioclase and clinopyroxene with resorbed boundary against oxide phases in coarser oxide gabbro, d. resorbed plagioclase, clinopyroxene, orthopyroxene and amphibole against oxide phases in coarser oxide gabbro, e. plagioclase, clinopyroxene and orthopyroxene resorbed by oxide phases in finer disseminated-oxide gabbro, f. Back-scatter electron image showing occurrence of symplectitic intergrowth associated with discrete magnetite grains. Abbreviations are as follows: Ol = olivine, Plag = plagioclase, Cpx = clinopyroxene, Opx = orthopyroxene, Amph = amphibole, Fe-Ti ox = Fe-Ti oxide, Mt = magnetite.

glass reference material (NIST SRM 614) is better than 4% in relative standard deviation for all elements. The analytical details and data quality are same as those outlined in Morishita et al. (2005).

4.2. Whole rock geochemistry

Whole rock analyses were carried out using fused glasses prepared from the rock powders by direct-fusion method. Details of sample preparation are same as those documented in Ichiyama et al. (2013) and Tamura et al. (2015). Major element analyses were obtained through EPMA at an accelerating voltage of 15 kV with 10 nA probe current and 30 µm probe diameter. The trace element concentrations were determined by LA-ICP-MS by ablating 100 µm diameter spots at 5 Hz repetition rate with energy density of 8 J cm^{-1} per pulse. External calibration standard used was BCR-2G (USGS glass reference material). The reference values were selected from GeoReM database (Jochum & Nohl, 2008). ^{42}Ca and CaO content were used as internal standard for data reduction. The accuracy and reproducibility of measurement were evaluated by measuring 7 fused glasses from powdered international reference materials (USGS and GSJ: gabbro, Iceland and Hawaii) viz. BHVO-2, BIR-1 and JGB-1, and is presented with the analyses.

5. Results

5.1. Mineral chemistry

5.1.1. Clinopyroxene

The interlayered rocks from Hole U1473A exhibit a considerable range of mineral compositions, consistent with the range of rock types recovered. Clinopyroxenes from the different lithology are found to be diospside and augite. While relatively primitive olivine gabbros and gabbros contain clinopyroxenes with much higher Mg# (ranges 85–70 in coarser olivine gabbros, 84–71 in finer olivine gabbros; 83–71 in coarser gabbros, 85–69 in finer gabbros), oxide-bearing lithologies are characterized by low Mg# (ranges 85–67 in coarser units and 83–65 in finer units) (Supplemental Table S2). Variation of clinopyroxene Mg#s with depth are plotted in Fig. 6a. A subtle upward decreasing trend is observed from the studied samples. Rims of coarse-grained clinopyroxenes display relatively low Mg# than their corresponding core (Figs. 7, 8a). However, Mg#s of finer clinopyroxenes span over a wider range, overlapping with that of the rims of coarse-grained clinopyroxenes (Figs. 7, 8a), (Supplemental Table S3). Clinopyroxene Mg# gradually increases away from the coarse–fine interface in both coarser and finer horizons (Fig. 8a).

The clinopyroxene compositions exhibit a crude array of plots for minor elements (Cr, Al, Ti, Na) with decreasing Mg# (Fig. 7) (Supplemental Table S2). Cr decreases abruptly with decreasing Mg# in olivine gabbro in both the coarser and finer lithologies (Fig. 7a). Almost the entire range of Cr_2O_3 is present in relatively primitive clinopyroxenes (Mg#> 80). However, this variation is not so rapid in gabbro and oxide bearing lithologies. Also, the Cr contents in the finer clinopyroxenes from the latter group are relatively low. Cr does not vary systematically from core to rim in any of the studied lithotypes (Fig. 7a). Al behaves similarly in both coarser and finer units (Fig. 7b). There is an overall decreasing trend of Al_2O_3 with decreasing Mg# in gabbros and oxide bearing rocks, whereas Al first increases and then decreases with decreasing Mg# in olivine gabbro. Although no variation is observed between core and rim of the coarser lithologies, finer horizons of gabbro and oxide bearing rocks have lower proportion of Al than the coarser variety (Fig. 7b). Variation of Na_2O with Mg# in olivine gabbro is similar to that of Al_2O_3 but it is not so obvious for other lithotypes (Fig. 7c). Proportion of Ti is relatively higher in the rim of the coarse grained clinopyroxenes (Fig. 7d, e). Nonetheless, it varies synonymously both in coarser and finer lithologies. TiO_2 first increases followed by sharp decline with decreasing Mg# (Fig. 7d). However, Cr_2O_3 and TiO_2 are poorly correlated with significant scattering (Fig. 7e).

In terms of trace elements clinopyroxenes from all lithotypes are characterised by relative depletion in LREEs compared to MREEs and HREEs (Fig. 9a – c). Also, clinopyroxenes from both coarser and finer horizons show small to marked negative anomalies in Eu, Sr and some HFSEs (e.g.- Zr) (Fig. 9a – c). Increase of Eu and Sr anomaly, and decrease of Zr anomaly with overall increase of trace element abundances irrespective of rock types is evident from Fig. 9. Overall trace element concentration in gabbro (sensu stricto) is relatively higher than that of olivine gabbro except for Sr (Fig. 9, Supplemental Table S4). Clinopyroxenes from finer olivine gabbro and oxide gabbros (sensu lato) however show enriched trace element signature than their coarser variety (Fig. 9a, c). Decrease of Eu/Eu* ($Eu_N[\sqrt{(Sm_N X Gd_N)}]$) with increasing clinopyroxene Zr content is a salient feature for both coarser and finer varieties of all lithotypes (Fig. 10). But Zr content which reaches up to ~70 ppm in finer olivine gabbros, is restricted to ~20 ppm in the coarser horizons of olivine gabbro.

5.1.2. Plagioclase

Plagioclase compositions span over a wide spectrum in the finer horizons, whereas it is relatively restricted in the coarser lithologies. There exists a fairly good correlation between the plagioclase compositions and various rock types recovered from Hole U1473A (Fig. 11) (Supplemental Table S5). Plagioclases with higher An contents are present in the olivine gabbros (ranges 73–44 in the coarser units and 69–45 in the finer units), followed by gabbros (in coarser units most of the data ranges 60–42 while one sample point has An content of 71, and in finer units ranges 60–44), and oxide-bearing lithologies (ranges 63–40 in coarser units, and 59–31 in finer units) as they become less calcic. Fig. 6b depicts that, plagioclase An content decreases slightly upward in the depth range of the investigated samples. Systematic core-rim variations in An content of the coarse-grained plagioclase are also evident from Fig. 8b. Felsic veins came across at certain horizons and we analysed the plagioclase grains present therein. They follow a com-

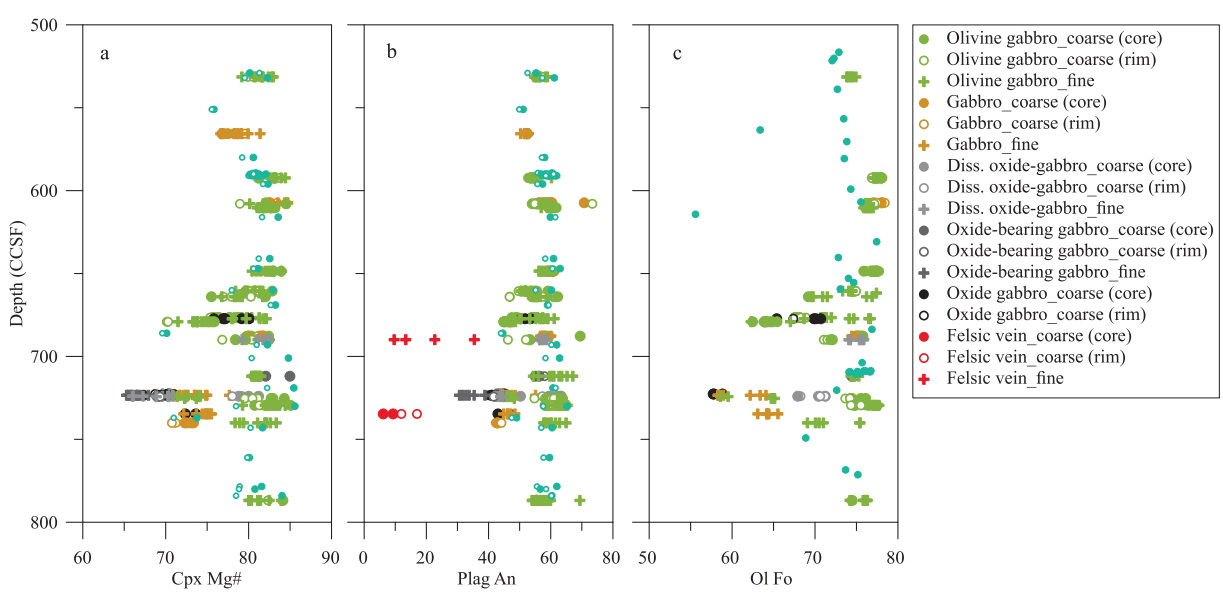

Fig. 6. Downhole mineral compositional variation of Hole U1473A lithologies. a. clinopyroxene Mg#, b. plagioclase anorthite content, c. olivine forsterite content. Small bluish circles from Zhang et al. (2020) are plotted for comparison of mineral compositions in the studied depth interval.

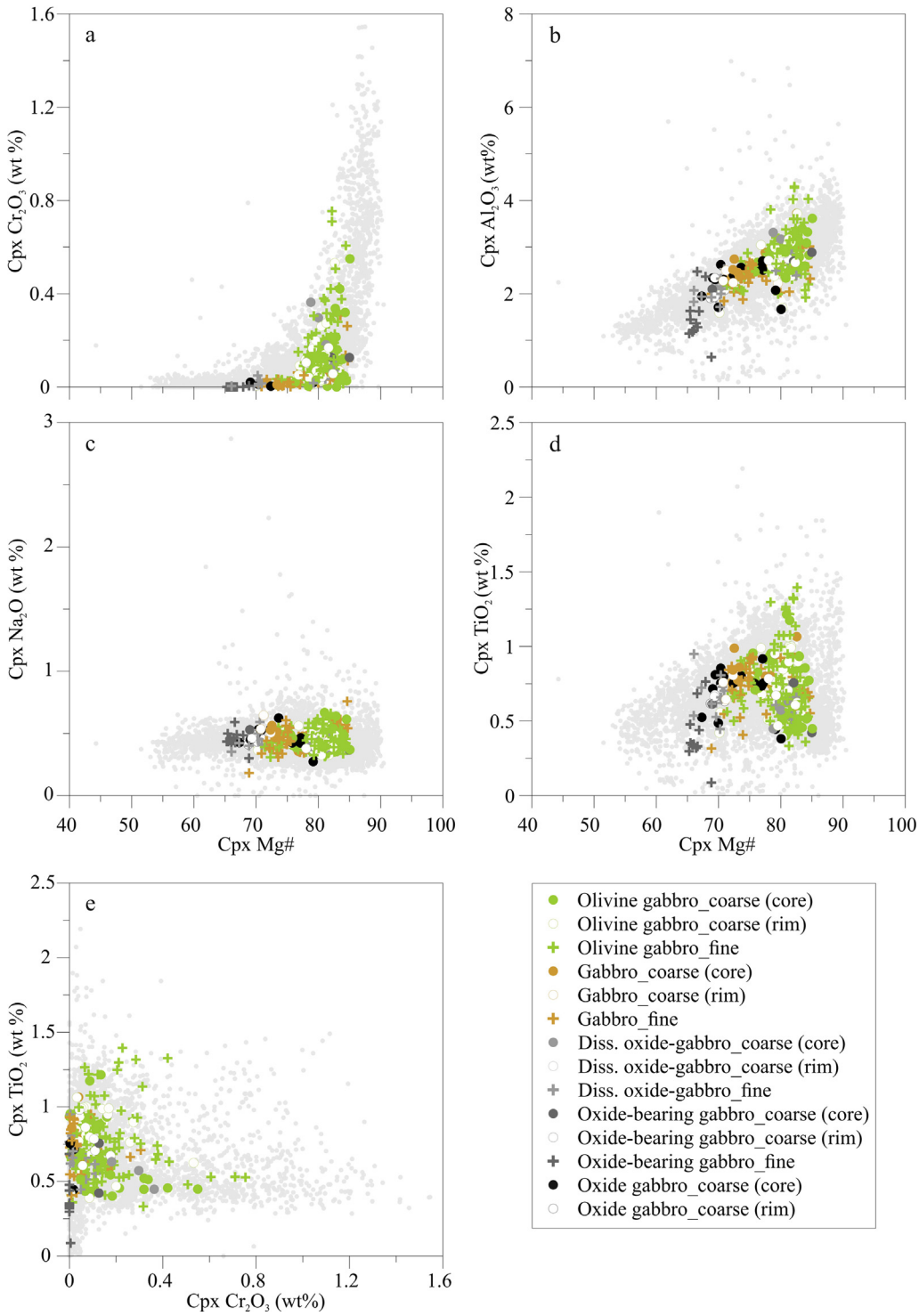

Fig. 7. a-d. U1473A clinopyroxene Mg# (=100* cationic Mg/[Mg + Fe], all Fe considered as Fe^{2+}) plotted against minor element concentrations, e. Cr_2O_3 vs TiO_2 of clinopyroxene. Cpx = clinopyroxene. Composition of clinopyroxene from ODP Hole 735B (Natland et al., 2002, Dick et al., 2002; Boulanger et al., 2020) and IODP Hole U1473A (Boulanger, 2020; Sanfilippo et al., 2020; Zhang et al., 2020, Ferrando et al., 2021a) have been plotted for comparison. Low total (<98.5 wt%) and high total (>101.5 wt%) data were excluded in this compilation.

pletely different trend in plagioclase An vs FeO* (all iron calculated as FeO) plot (Fig. 11). These plagioclases are characterized by significantly low An content (35–10 An mol% and 17–9 An mol% in coarser and finer units respectively) (Fig. 11). Olivine gabbros, gabbros and oxide-bearing lithologies exhibit a fairly good correlation between plagioclase An content and FeO*, as FeO decreases with decreasing An content from olivine gabbros to its evolved counterparts (Fig. 11).

5.1.3. Olivine

Olivine Fo content ranges 78–62 in coarser olivine gabbro and 78–59 in their finer counterparts; 78–77 in coarser gabbros and 78–75 in finer gabbros; 75–58 in coarser oxide bearing lithologies Supplemental Table S6). Range of olivine Fo content in the finer units of oxide bearing lithologies is difficult to constrain due to its rare occurrences in these horizons. No significant downhole or core-rim compositional variation is evident in olivine (Fig. 6c,

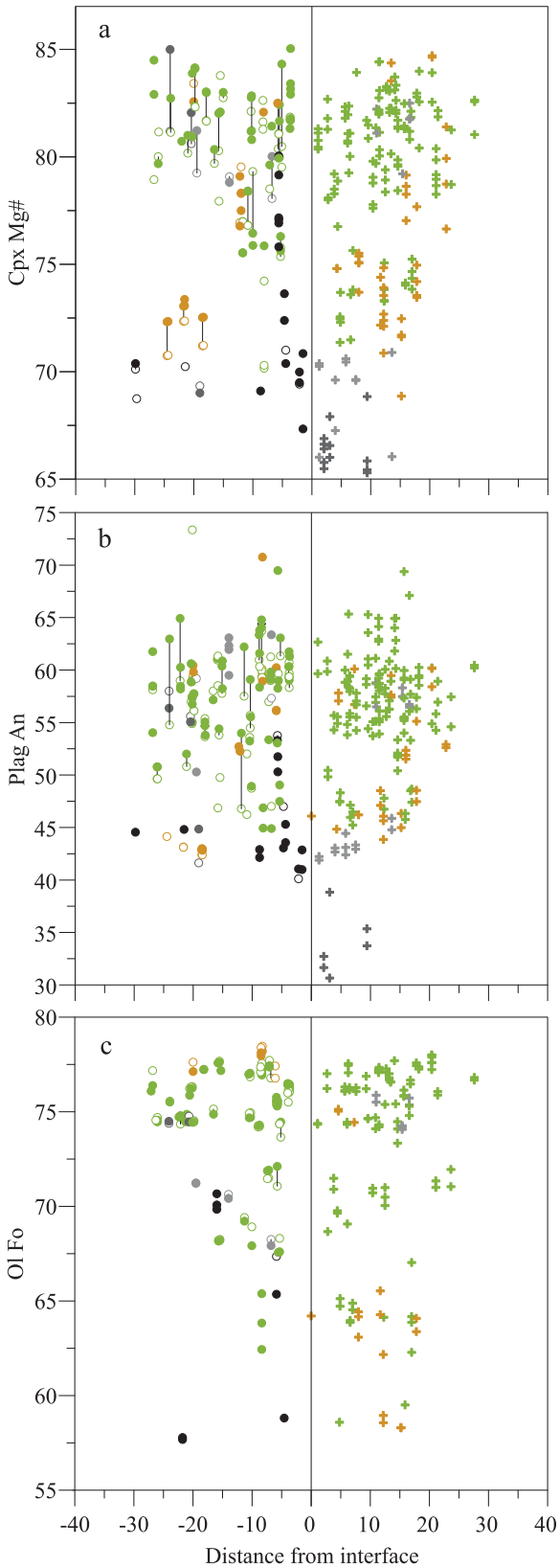

Fig. 8. Variation of mineral compositions for different rock types [a. cpx, b. plag, c. ol] across grain-size contacts. Composition of coarse-grained domains are plotted in the left and that of the fine-grained domains are plotted in the right. Core-rim analyses from the same grain are connected by a tie line. Abbreviations are as follows: Ol = olivine, Plag = plagioclase, Cpx = clinopyroxene. Symbols are same as in Fig. 6.

8c). Although having overlapping compositional variation there is a good correlation between the olivine compositions and rock types recovered from Hole U1473A (Fig. 12 a, b). The most magnesian olivines are chiefly present in the olivine gabbros and become eventually Mg-poor towards oxide-bearing gabbros and oxide gabbros (Fig. 12a, b). Finer units of the oxide-bearing lithologies are commonly devoid of olivine. The NiO content in olivine show a positive (Fig. 12a) and that of MnO shows a tight negative correlation (Fig. 12b) with Fo content irrespective of the coarse and fine lithologies.

5.1.4. Amphibole

Amphiboles are mostly pargasite with few samples found to be tremolite and hornblende (Fig. 13a). Mg# of pargasitic amphiboles ranges 79–68 in coarser olivine gabbros, 77–76 in finer olivine gabbros; 72–69 in finer gabbros; while in oxide bearing lithologies it ranges 79–61 and 78–65 in the coarser and finer intervals respectively (Supplemental Table S7) (Fig. 13). Amphiboles with high Al_2O_3, Na_2O and TiO_2 and low SiO_2 are interstitial in nature (Fig. 13-b-e), similar to the amphibole blebs as noted by Coogan et al. (2001) from other ocean ridges. Replacive amphiboles are characterised by scattered compositions with relatively higher SiO_2 (Fig. 13b, e). Positive correlations between Al_2O_3 and Na_2O, TiO_2 and a negative correlation between Al_2O_3 and SiO_2 are evident in Fig. 13. However, no such correlations are recorded between Mg# and SiO_2, and Al_2O_3 contents (Fig. 13e, f).

5.2. Whole rock geochemistry

5.2.1. Olivine gabbro and gabbro

Hole U1473A olivine gabbros are characterised by high Mg# [(100* cationic Mg/(Mg + Fe)] (ranges 79–73 in coarser and 78–69 in finer lithologies), as well as high Ca# [100*cationic Ca/(Ca + Na)] which ranges 78–68 in coarser and 79–68 finer lithologies (Fig. 14a) (Supplemental Table S8). Whereas, in gabbros, Mg# ranges 79–69 (Fig. 14a, b, c, d) and Ca# ranges 76–67 (constrained from a few samples) (Fig. 14a). These rocks broadly exhibit differentiation trends in Mg# vs Ca# and other minor element (Cr, Ni, Y) plots. Ca#, Cr and Ni decreases with decreasing Mg#, while Y covaries negatively with Mg# (Fig. 14 a, b, c, d). Olivine gabbros and gabbros are characterised by relatively higher concentration of compatible elements (e.g.- Ni ranges 176–46 ppm in coarser olivine gabbros, 143–50 ppm in finer olivine gabbros and 140–83 ppm in gabbros) and lower concentration of incompatible elements (e.g., Yb ranges 2.63–0.49 ppm in coarser olivine gabbros, 1.09-0.76 ppm in finer olivine gabbros and 1.24–0.59 ppm in gabbros) compared to other evolved lithologies recovered from Hole U1473A. Olivine gabbros and gabbros are depleted in LREE (Cl chondrite normalised La/Yb ranges 0.77–0.31 in coarser olivine gabbros, 0.57–0.28 in finer olivine gabbros and 0.36–0.33 in gabbros) and also in HFSE (e.g.- Zr/Sm ranges 23.31–11.04 in coarser olivine gabbros, 18.67–10.02 in finer olivine gabbros and 12.75–8.29 in gabbros) (Fig. 14 a, b). They are also depleted in highly incompatible trace elements (Nb/Zr ranges 0.029–0.006 in coarser olivine gabbros, 0.013–0.003 in finer olivine gabbros and 0.011–0.005 in olivine gabbros and gabbros) (Supplemental Table S8).

The finer intervals of olivine gabbro are relatively enriched in trace element than the coarser domains (Fig. 15a). Two coarse-grained olivine gabbro samples in Fig. 15a have elevated trace element abundances than the rest, likely due to the presence of late-magmatic phases (e.g.- orthopyroxene, amphibole) in those samples (sample no.- 75R-1 W-26/33(c) and 78R-7 W-23/30(c)). Both olivine gabbros and gabbros exhibit marked positive Sr and Eu anomalies (Fig. 15a, b). Sr/Sr* ($Sr_N[\sqrt{(Ce_N X Nd_N)}]$ ranges 9.64–1.05

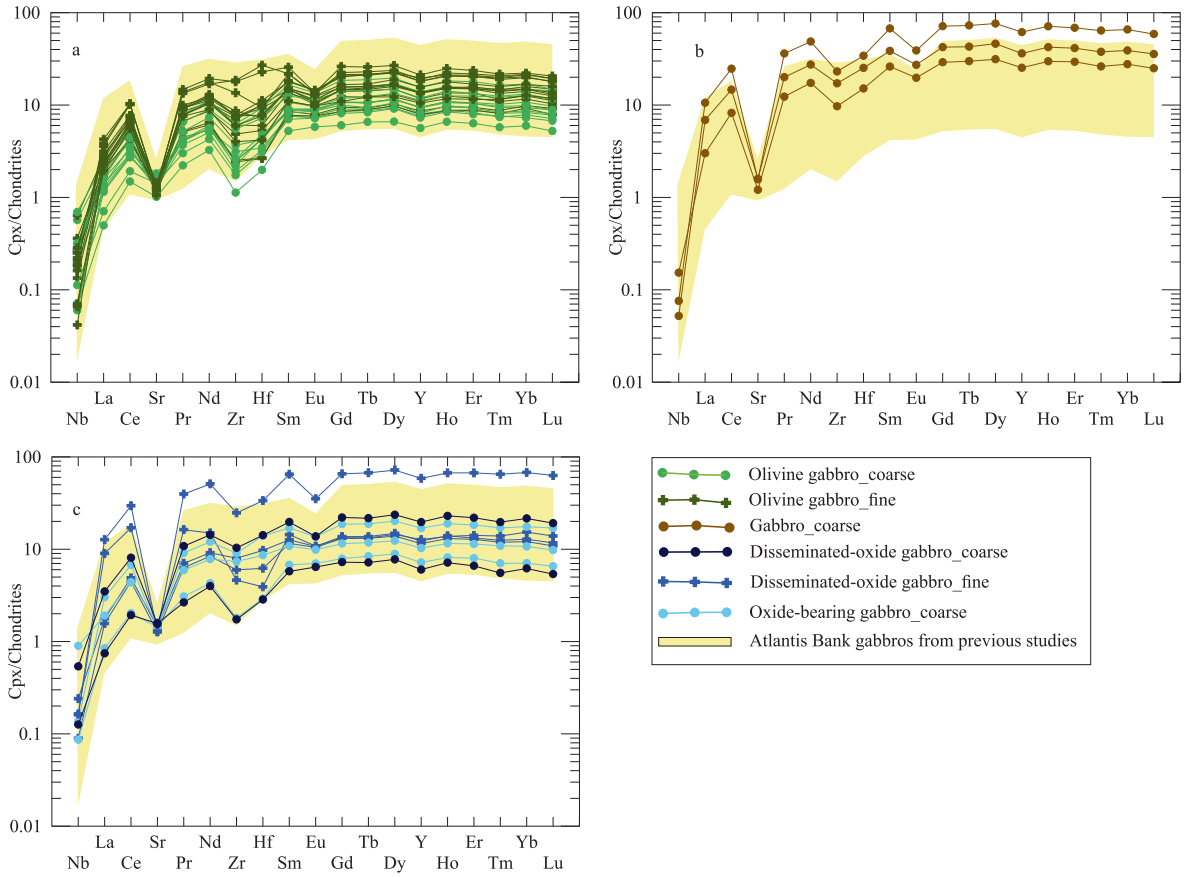

Fig. 9. Trace element patterns of clinopyroxenes in a. olivine gabbros, b. gabbros, c. oxide bearing lithologies from U1473A and their variations in the coarser and finer units. Normalising values are taken from McDonough & Sun (1995). Trace element compositions from Hole 735B (Boulanger, 2020, Boulanger et al., 2020) and Hole U1473A (Boulanger, 2020; Boulanger et al., 2020; Sanfilippo et al., 2020; Zhang et al., 2020, Ferrando et al., 2021a) have been used for comparison.

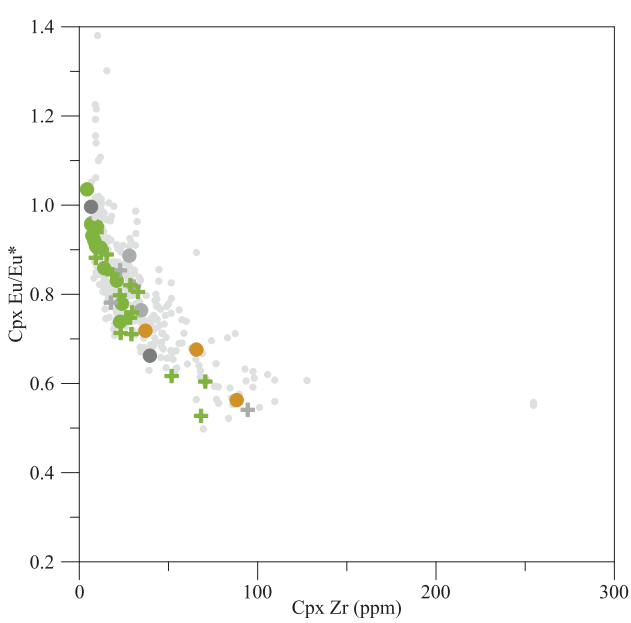

Fig. 10. Plot of Eu/Eu* against Zr of U1473A gabbro clinopyroxenes. Note the strong decrease of Eu/Eu* with increasing Zr concentrations. Trace element compositions from Hole 735B (Boulanger 2020, Boulanger et al., 2020) and Hole U1473A (Boulanger, 2020; Boulanger et al., 2020; Sanfilippo et al., 2020; Zhang et al., 2020, Ferrando et al., 2021a) have been used for comparison. Symbols are same as in Fig. 6.

in olivine gabbros from coarser horizons, 6.92–3.79 in finer horizons and 9.02–4.35 in gabbros. Eu/Eu* ($Eu_N[\sqrt{(Sm_N x Gd_N)}$ ranges 2.29–0.88 in coarse-grained olivine gabbros, 1.64–1.28 in fine-grained olivine gabbros and 1.79–1.38 in gabbros.

5.2.2. Oxide bearing lithologies

Oxide bearing lithologies are typically characterised by low Mg# (ranges 71–49 in coarser and 75–51 in finer lithologies), high FeO (ranges 14.5–7 wt% and 12.7–5.4 wt% in coarser and finer lithologies respectively) and TiO_2 content (ranges 2.8–0.2 wt% and 2.7–0.3 wt% in coarser and finer lithologies respectively) (Supplemental Table S8). Variations of bulk Ca#, Cr, Ni and Y with Mg# show differentiation trends among these rock groups following olivine gabbros and gabbros (Fig. 14a, b, c, d). These rocks are overall enriched in trace elements compared to olivine gabbro and gabbro (Yb ranges 5.14–0.44 ppm and 4.32–0.93 ppm in coarser and finer units respectively) (Fig. 15). Finer varieties show somewhat enriched trace element than the coarser ones (Fig. 15c). One sample (sample no. 82R-2 W/125–132 (c)) in Fig. 15c is distinctly enriched of Zr and Hf. Modal abundances of orthopyroxene and oxide phases in this sample is remarkably high. Fractionation of LREE relative to HREE in these rocks is comparable to olivine gabbros and gabbros (Cl chondrite normalised La/Yb ranges 0.68–0.38 and 0.48–0.43 in coarser and finer units respectively). Furthermore, oxide-bearing lithologies are also characterised by marked positive Eu and Sr anomalies (Fig. 15c) (Eu/Eu* ($Eu_N[\sqrt{(Sm_N x Gd_N)}$ ranges 2.72–1.1 and 1.57–1.11 in coarser and finer units respectively; Sr/Sr* ($Sr_N[\sqrt{(Ce_N x Nd_N)}]$ ranges 11.21–0.82 and 5.66–1.05 in coarser and finer units respectively). Nonetheless, they are

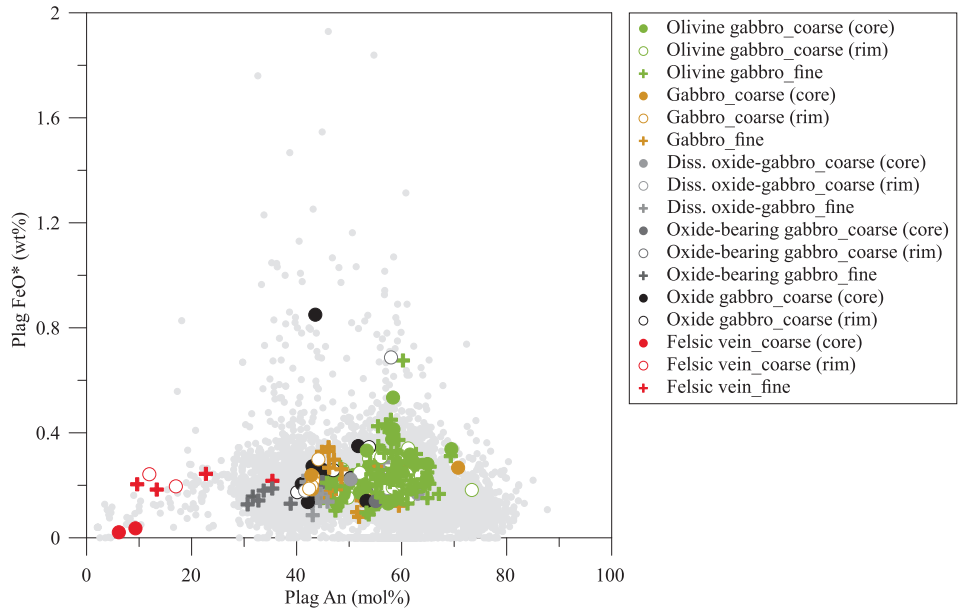

Fig. 11. Plagioclase anorthite content vs FeO* (all iron as FeO) plot of U1473A gabbros. Plagioclase compositions from ODP Hole 735B (Natland et al., 2002; Boulanger et al., 2020) and IODP Hole U1473A (Boulanger, 2020; Boulanger et al., 2020; Sanfilippo et al., 2020; Zhang et al., 2020, Ferrando et al., 2021a) is plotted for comparison. Low total (<98.5 wt%) and high total (>101.5 wt%) data were excluded in this compilation.

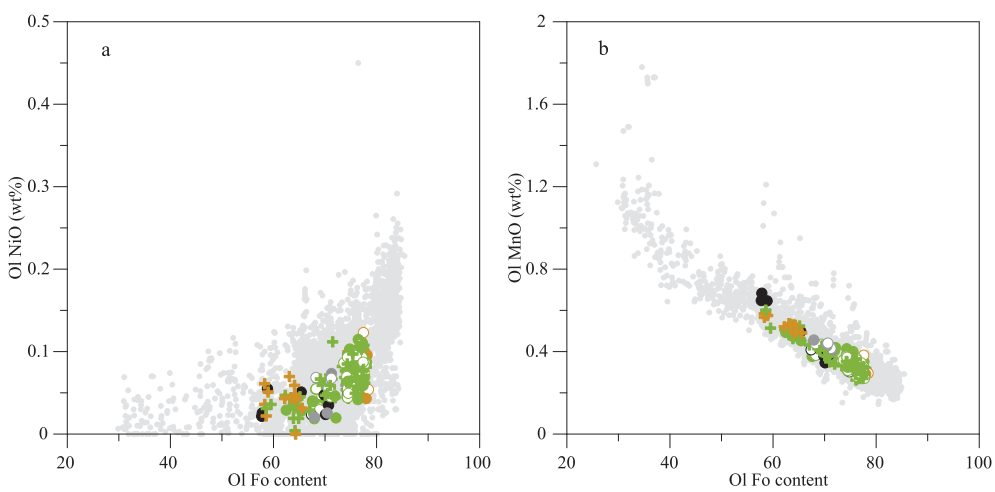

Fig. 12. a. NiO and b. MnO plotted against forsterite content of olivine of U1473A gabbros. Symbols are same as in Fig. 6. Compositions of olivine from ODP Hole 735B (Natland et al., 2002; Boulanger et al., 2020) and IODP Hole U1473A (Boulanger, 2020; Boulanger et al., 2020; Sanfilippo et al., 2020; Zhang et al., 2020, Ferrando et al., 2021a) is plotted for comparison. Low total (<98.5 wt%) and high total (>101.5 wt%) data were excluded in this compilation.

depleted in Zr compared to REE (Zr/Sm ranges 138.53–11.53 and 14.69–12.16 in coarser and finer units respectively) and highly incompatible trace elements (Nb/Zr ranges 0.021–0.005 and 0.031–0.007 in coarser and finer units respectively) (Supplemental Table S8) akin to olivine gabbros and gabbros.

6. Discussion

The magmatic accretion in the Atlantis Bank OCC is thought to be constructed by repeated cycles of intrusion. Recovered crustal section from Hole 735B represents five such episodic cycles (Dick et al., 2000; Natland and Dick, 2002). In contrast, three cycles have been identified from Hole U1473A (Dick et al., 2019b; Boulanger et al., 2021) (Fig. 2); each marked by broad upward differentiation trends with decreasing Mg#, Cr and Ni contents and increasing Y content from the base of every overlying unit (Dick et al., 2017; Zhang et al., 2020). Since grain-size variation is more pronounced at the lower part of the hole and the sampling was strategically targeted to the layer (grain size) interfaces, the studied samples all belong to a single geochemical cycle. This poses robustness of any modelling approach that can be exercised based on these samples because each cycle likely behaved like a closed system with no fresh melt input.

6.1. Layering at Atlantis Bank

Igneous layering in plutonic igneous bodies can be developed by various processes, like convection (Hess, 1960; Engell, 1973; Chen and Turner, 1980; Barriere, 1981; Huppert and Sparks, 1984; Kogarko and Khapaev, 1987; Naslund and McBirney, 1996), differential settling velocities of minerals with varying density and grain-size (McBirney and Noyes, 1979; Naslund and McBirney, 1996) or rapid changes in intensive parameters viz. tem-

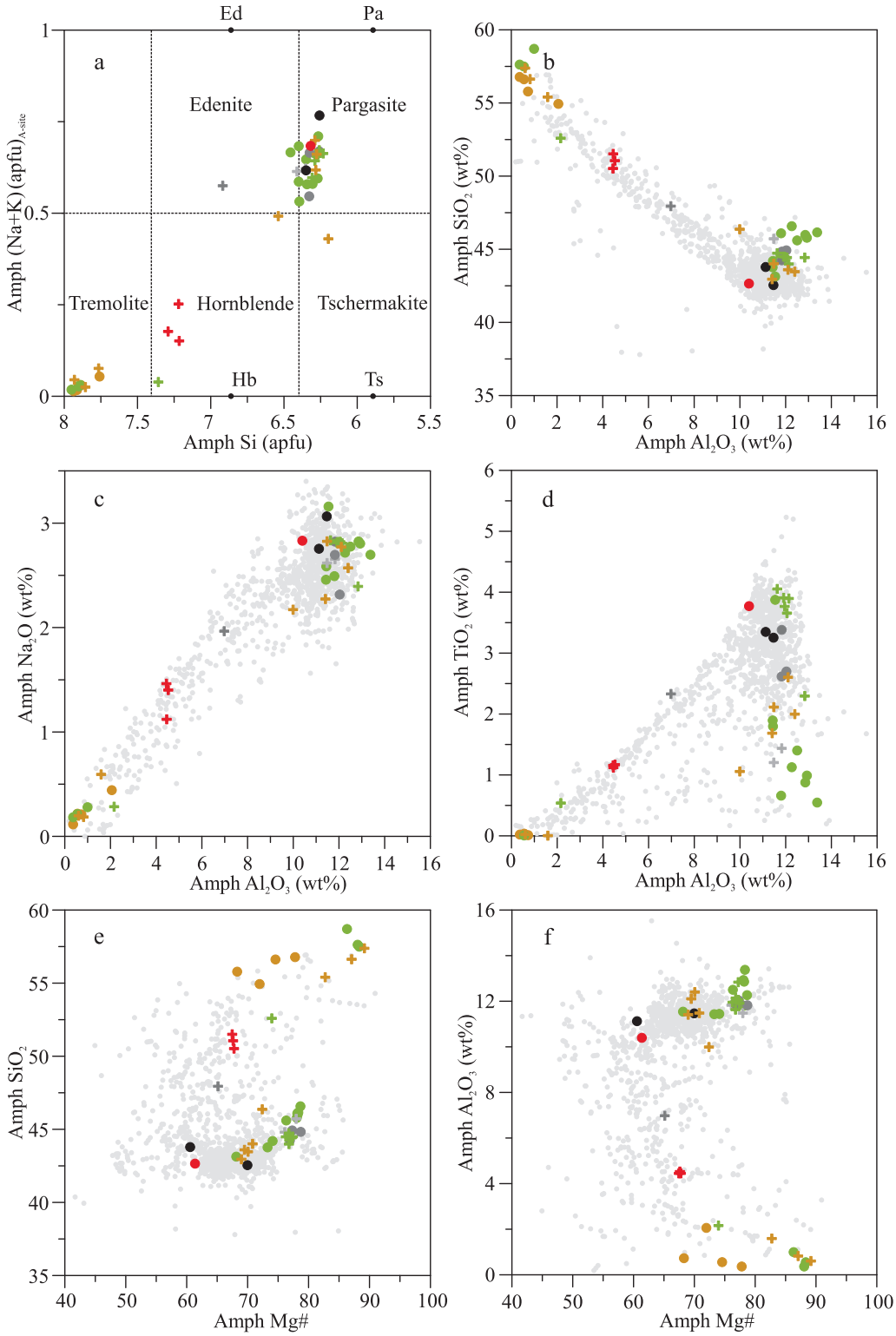

Fig. 13. a. Classification of Hole U1473A amphiboles, b. - f. Variation of Major and minor element parameters in amphiboles. Variations of Al_2O_3 with b. SiO_2, c. Na_2O, d. TiO_2 and Mg# with e. SiO_2, f. Al_2O_3. Symbols are same as in Fig. 10. Compositions of amphibole from ODP Hole 735B (Natland et al., 2002) and IODP Hole U1473A (Nguyen et al., 2018) have been plotted for comparison.

perature, pressure, oxygen fugacity, crystal nucleation and growth rate (Hort et al., 1993; Naslund & McBirney, 1996) etc. Ubiquitous presence of grain-size layering within the lower crustal lithotypes at Atlantis Bank is well documented from Hole 735B (Bloomer et al., 1991; Dick et al., 2000), Hole 1105A (MacLeod et al., 2017) and Hole U1473A (Dick et al., 2017; Boulanger et al., 2021, Ferrando et al., 2021a). Intrusion of fine-grained material within otherwise coraser horizons is evident from the contact relationships depicted in Fig. 3. Migration of melt in an environment with high melt fraction probably leads to diffuse contacts (Fig. 3a)

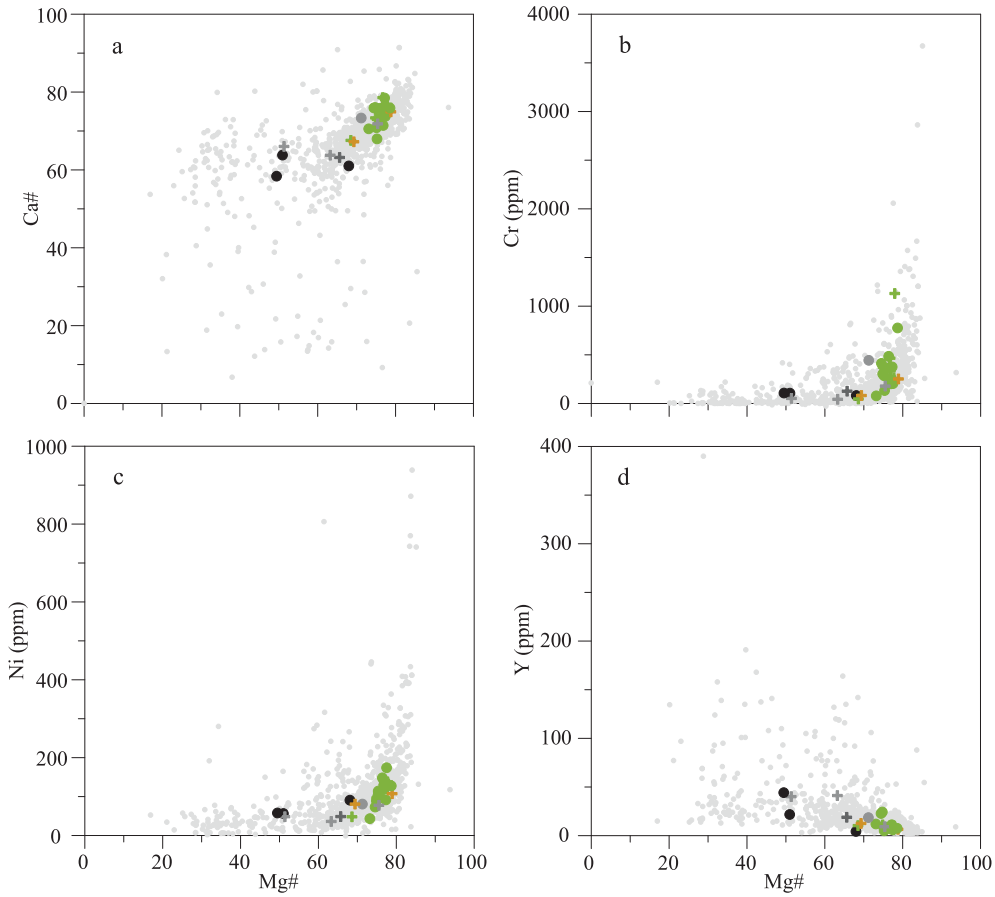

Fig. 14. Variation of whole rock Mg# (100* cationic Mg/[Mg + Fe], all Fe considered as Fe^{2+}) with minor elements from U1473A gabbros. a. Ca#, b. Cr, c. Ni decreases; while d. Y increases systematically with decreasing Mg#. Symbols are same as in Fig. 6. Whole rock data from ODP Hole 735B (Natland et al., 2002) and recent IODP Hole U1473A (MacLeod et al., 2017; Zhang et al., 2020) have been plotted for comparison.

(Collier and Kelemen, 2010; Van den Bleeken et al., 2011; Saper and Liang, 2014). On the contrary, sharp contacts (Fig. 3b) are developed when focused melt migration takes place at a low melt/rock ratio as pointed out by Ferrando et al. (2021a) from this hole. Niu et al. (2002) proposed several possible mechanisms that might led to the grain-size variations recorded in the adjacent Hole 735B. Intrusion of a new melt into the solidifying coarse-grained crystal mush may cause such grain-size inhomogeneity. This requires a substantial time difference between the crystallization of the coarser and finer horizons, and likely should have been reflected by a change in parental melt compositions corresponding to them. This is in consistent with the findings of Boulanger et al. (2021) who have proposed that, the coarser and finer lithologies in Hole U1473A are crystallized from two chemically distinct melt. While calculating Mg# of melt in equilibrium with both the coarse- and fine-grained clinopyroxene, using the Fe–Mg distribution formulation of clinopyroxene-melt (Equation 11 of Bédard, 2010) we found relatively lower values for the fine-grained lithologies. Equilibrium melt Mg#s of cores of coarse-grained clinopyroxenes from olivine gabbros, gabbros and oxide-bearing gabbros range 62–46, 58–40 and 62–34 respectively, whereas in the finer layers these range 60–39, 60–36 and 58–32 respectively. Comparable melt Mg# of the rims of the coarse-grained clinopyroxenes (ranges 60–38 in olivine gabbros, 58–39 in gabbros and 55–36 in oxide-bearing rocks) with those of the fine-grained lithologies is noteworthy. Also, calculated trace element compositions of melts in equilibrium with clinopyroxenes from finer olivine gabbros and oxide-bearing rocks are slightly enriched than their coarser variety (Fig. 16a, c) (Supplemental Table S9). This indicates parental melt composition of the finer lithology is somewhat evolved than that of the coarse-grained rocks. We have also probed the variations of incompatible trace elements between the coarse- and the fine-grained clinopyroxenes (Fig. 17). The clinopyroxenes from the finer horizons are somewhat enriched in elements like Hf (Fig. 17a) and Zr (Fig. 17b). Moreover, fractionation of LREE with respect to HREE is higher in finer lithologies (Fig. 17c).

Alternatively, the grain-size heterogeneity recorded from Atlantis Bank gabbros could be the result of variation in nucleation and crystal growth rates (Bloomer et al., 1991; Niu et al., 2002, Ferrando et al, 2021a). Nucleation is principally controlled by two factors; Gibbs free energy of forming a nucleus and material transportation rate from liquid onto the developing crystal (Dowty, 1980; Brandeis et al., 1984). These two in turn depend on the degree of undercooling (Kirkpatrick, 1975; Kirkpatrick et al., 1976; Kirkpatrick, 1977; Dowty, 1980; Brandeis et al., 1984). Due to continuous change in liquid composition during fractional crystallization, degree of undercooling decreases with decreasing phase-saturation temperature (Mollo and Hammer, 2017). This leads to the prevalence of crystal growth over nucleation. Then undercooling may increase owing to the removal of latent heat of crystallization, and nucleation become the dominating mechanism to carry out the process of crystallization (Kirkpatrick et al., 1976; Dowty, 1980).

Clinopyroxene and plagioclase of the studied coarse-grained gabbros (sensu lato) exhibit slightly evolved rim composition than their corresponding core (Figs. 7, 8, 11). The fine-grained crystals however show large compositional variations, ranging from as primitive as the core composition of the coarse-grained crystals

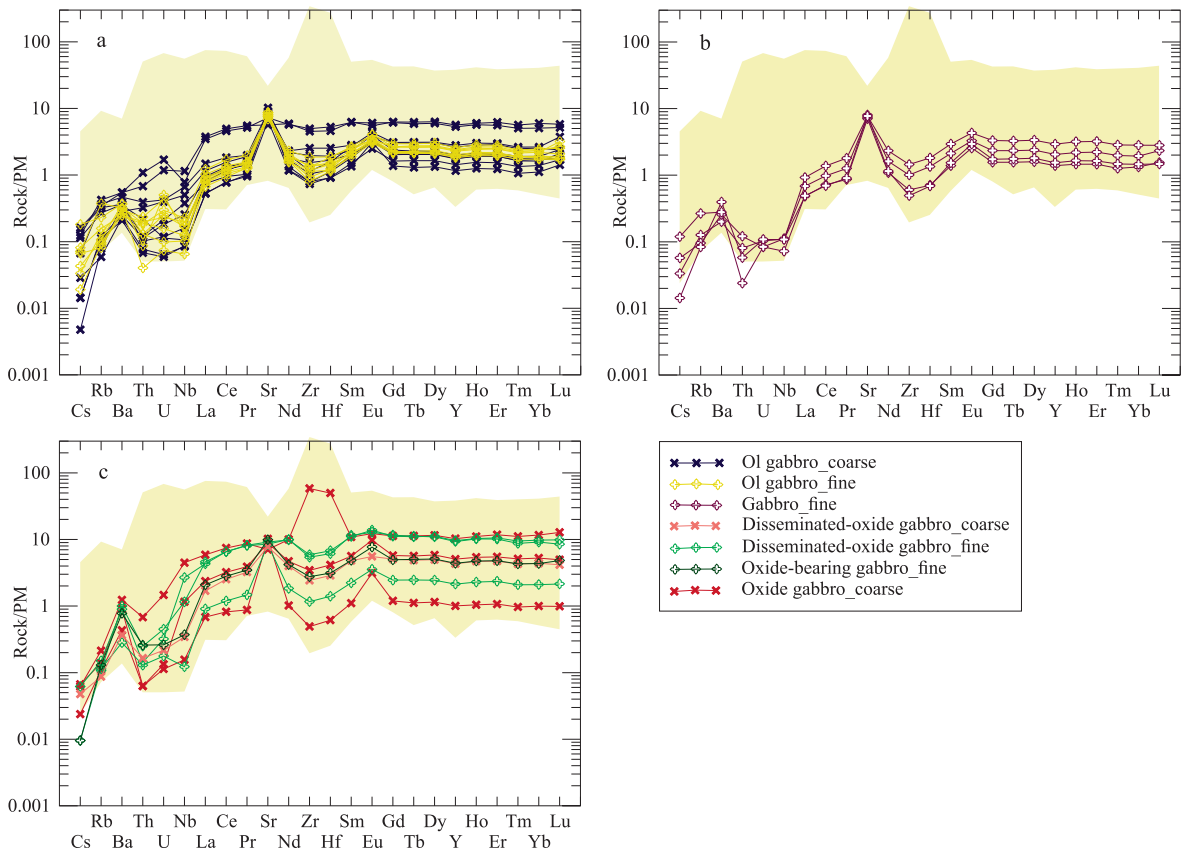

Fig. 15. Bulk trace element compositions normalised to primitive mantle values of different rock types recovered from Hole U1473A a. olivine gabbros, b. gabbros, c. oxide bearing lithologies. Normalizing values are taken from McDonough and Sun (1995). Whole rock trace element data from ODP Hole 735B (Natland et al., 2002) have been plotted.

to more evolved than their rim (Fig. 8). We suggest that, the cores of the coarse-grained crystals were crystallized at the initial stage of cooling at lower degree of undercooling. This condition prevailed as the crystals continued to grow in size and their respective rims became evolved in composition by reacting with the interstitial melt. Since the composition of the residual melt progressively changes it does not remain akin to that of the growing crystals. Additionally, removal of the latent heat of crystallization from the system would develop a compositional and temperature gradient near the crystals (Kirkpatrick, 1977). This is consistent with the intragrain compositional variations thoroughly recorded from this study. Ferrando et al. (2021a) have illustrated the differences in equilibrium temperature between the core and rim of the corase-grained crystals. These lines of evidences suggest that the temperature continued to decrease gradually during the formation of coarse-grained horizons. This was accompanied by the progressive decrease of liquidus temperature owing to the change in melt composition (Ferrando et al., 2021a). This thermal evolution of the system might have severely impeded the degree of undercooling, leading to crystal growth being the predominant process of crystallization. The melts intercumulus to the solidifying crystal mush expelled as a result of compaction or filter pressing and segregated into horizons devoid of crystals (Ferrando et al., 2021a).

6.2. Possible mechanisms for lower crust formation at Atlantis Bank

6.2.1. Fractional crystallization

Earlier investigations suggest that Atlantis Bank lithologies (as recovered from Hole 735B) represent a general differentiation trend from a parental MORB (Dick et al., 2000; Boulanger et al., 2020). Natland and Dick (2002) interpreted all the olivine gabbros and gabbros to be adcumulates with < 7% interstitial melt (<2% in most of the cases) and most of the oxide gabbros (sensu lato) to be mesocumulates and orthocumulates with relatively greater proportion of interstitial melts.

6.2.1.1. Evidence from mineral chemistry. Clinopyroxene Mg#s of the Hole U1473A gabbros (senstu lato) vary over a wide range (94 in olivine gabbros to 66 in oxide rich gabbros) indicating their parental melts range from primitive to evolved in composition. Sharp decrease of clinopyroxene Cr_2O_3 with decreasing Mg# (Fig. 7a) reflects compatible nature of Cr. Variation of Al_2O_3 to Mg# (Fig. 7b) might be related with plagioclase fractionation. Initial increase followed by steady decrease of clinopyroxene TiO_2 with lowering Mg# (Fig. 7d) is hallmark for fractional crystallization of gabbroic assemblage. Ti preferably remains in the melt phase during cotectic crystallization of olivine, plagioclase, and pyroxene followed by the crystallization of oxide-bearing phases when Fe-Ti oxide appears on liquidus. The strong decrease of Eu/Eu* with increasing Zr (Fig. 10) in clinopyroxene indicates enrichment of trace element, related to a decrease in melt mass as plagioclase fractionated. Uniform decrease of olivine NiO with decreasing Fo content in both coarser and finer lithologies (Fig. 12a) is consistent with the strong affinity of Ni for olivine and its depletion in the melt with the onset of fractional crystallization. However, variation of MnO with olivine Fo content (Fig. 12b) reflects its incompatible behaviour in olivine. Decrease of FeO* in plagioclase from olivine gabbros to oxide-gabbros with decreasing plagioclase An content (Fig. 11) is typical for fractional crystallization in gabbroic assemblage. However, the plagioclases in the felsic veins follow a differ-

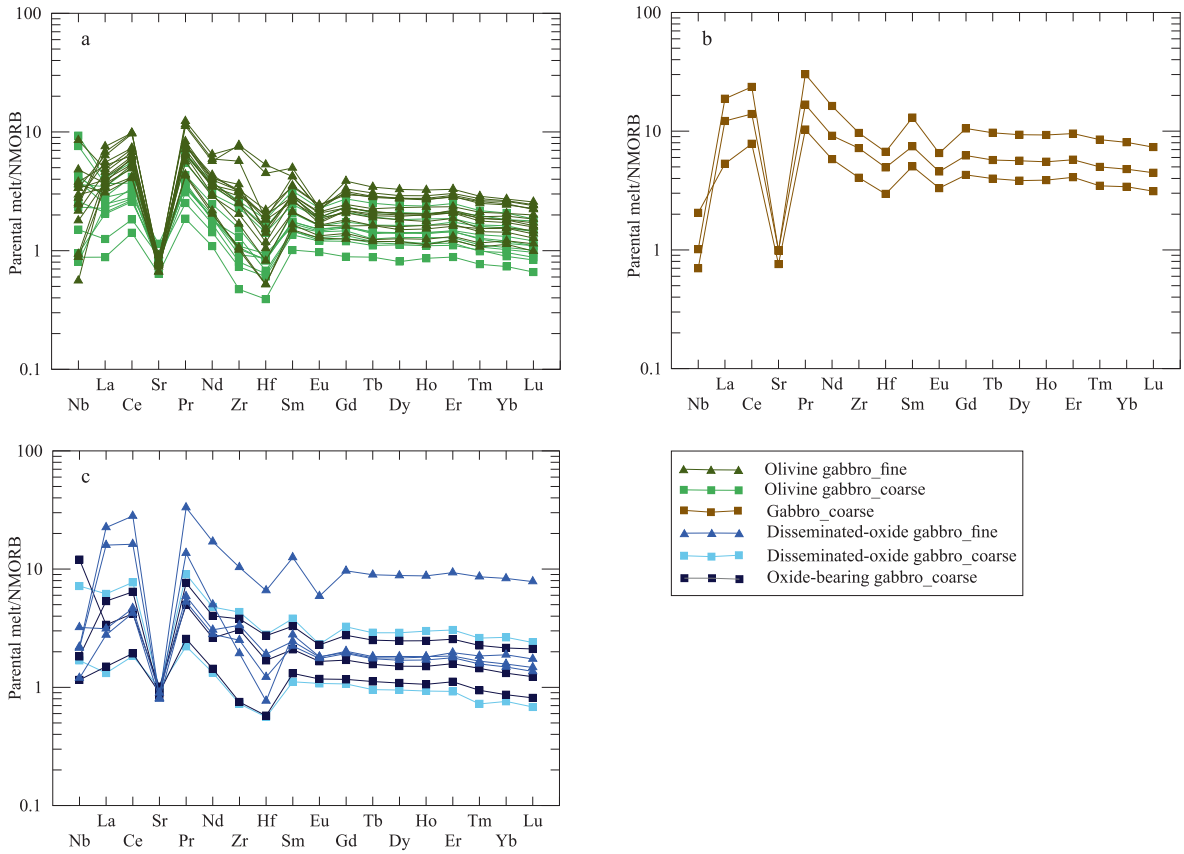

Fig. 16. Trace element patterns of calculated equilibrium melts of U1473A clinopyroxenes. Normalising values are taken from Sun & McDonough (1989).

ent trend from the gabbros and they usually contain more FeO* than the oxide-bearing gabbros (sensu lato) (Nguyen et al., 2018). Such correlation is also recorded in Dick et al. (2002), and may record variable oxidation conditions (France et al., 2010).

Fig. 18 depicts significant correlations between plagioclase An content, Mg# of clinopyroxene, orthopyroxene, and olivine Fo content of the studied samples suggesting chemical equilibrium among these phases (Supplemental Tables S2, S5, S6, S10). Dick et al. (2002) interpreted fractionation of different constituent phases along olivine-plagioclase, olivine-plagioclase-clinopyroxene and plagioclase-clinopyroxene-oxide ± olivine cotectics as the root cause for similar correlations in Hole 735B cumulates. They further inferred that, plagioclase and other silicate phases were precipitated from a common melt during the course of fractional crystallization. However, Niu et al. (2002) argued that, albeit the presence of oxide phases in some of the samples, they are not in equilibrium with the silicate phases as their compositions are not correlatable to those of silicates. A corollary of this finding is that, the oxide phases are not crystallized from the same melt as the silicate minerals did but likely from a more evolved percolating melt (Niu et al., 2002).

6.2.1.2. Evidence from whole rock geochemistry. Hole U1473A gabbros (sensu lato) are characterized by downhole variation of various differentiation indices, like whole rock Mg#, Ca# and trace elements Cr, Ni, and Y with major discontinuities occurring at ~ 60–90, ~300, and ~ 700 m CCSF (Dick et al., 2017; MacLeod et al., 2017). This variation perhaps resulted from cyclic intrusions of new magma batches, where chemically primitive olivine, pyroxene, along with low amount of evolved trapped melt accumulated at the base of each intrusion resulting high Mg#, Ca# and Cr and Ni concentrations (MacLeod et al., 2017). Such geochemical cycles are also reported from Hole 735B (Dick et al., 2000, 2002). Cr and Ni in the present study have significantly higher concentration in olivine gabbros and gabbros compared to oxide-bearing rocks (Fig. 14b, c), whereas abundance of Y is relatively low in olivine gabbros (Fig. 14d). This variation is consistent with the compatible behaviour of Cr, Ni and incompatible nature of Y during fractionation of MORB. As evident from Mg# vs Ca# plot (Fig. 14a), oxide-gabbros do not follow the linear trend defined by olivine gabbro, gabbro, disseminated-oxide gabbro and oxide-bearing gabbro reflecting higher clinopyroxene abundances in this rock (Dick et al., 2019b). Marked positive Eu and Sr anomalies (Fig. 15a, b, c) of all lithounits are indicative of their cumulative origin.

6.2.2. Reactive porous flow

6.2.2.1. Petrological evidence. Hole U1473A rocks are crystallized from a wide range of melt, starting from relatively primitive to evolved in composition as indicated by their texture and variations in phase and bulk chemical compositions. Poikilitic and ophitic to sub-ophitic habits of olivine, clinopyroxene and plagioclase are commonly observed, which indicate simultaneous crystallization of these phases. Irregular plagioclase chadacrysts with resorbed to sharp grain boundaries enclosed by clinopyroxene (Fig. 4a, b, e) is omnipresent in the coarser and finer varieties of olivine gabbro. This textural feature is observed ubiquitously in the oceanic gabbros (Lissenberg and Dick, 2008; Lissenberg et al., 2013; Lissenberg and MacLeod, 2016; Zhang et al., 2020; Boulanger et al., 2020, 2021; Ferrando et al., 2021a, 2021b) indicating a reaction in which plagioclase was dissolving with simultaneous crystallization of clinopyroxene. Occurrences of large olivine oikocrysts enclosing plagioclase with resorbed contacts (Fig. 4c) also indicate dissolution process. Corroded olivine chadacrysts with irregular boundaries enclosed by clinopyroxene (Fig. 4d) sug-

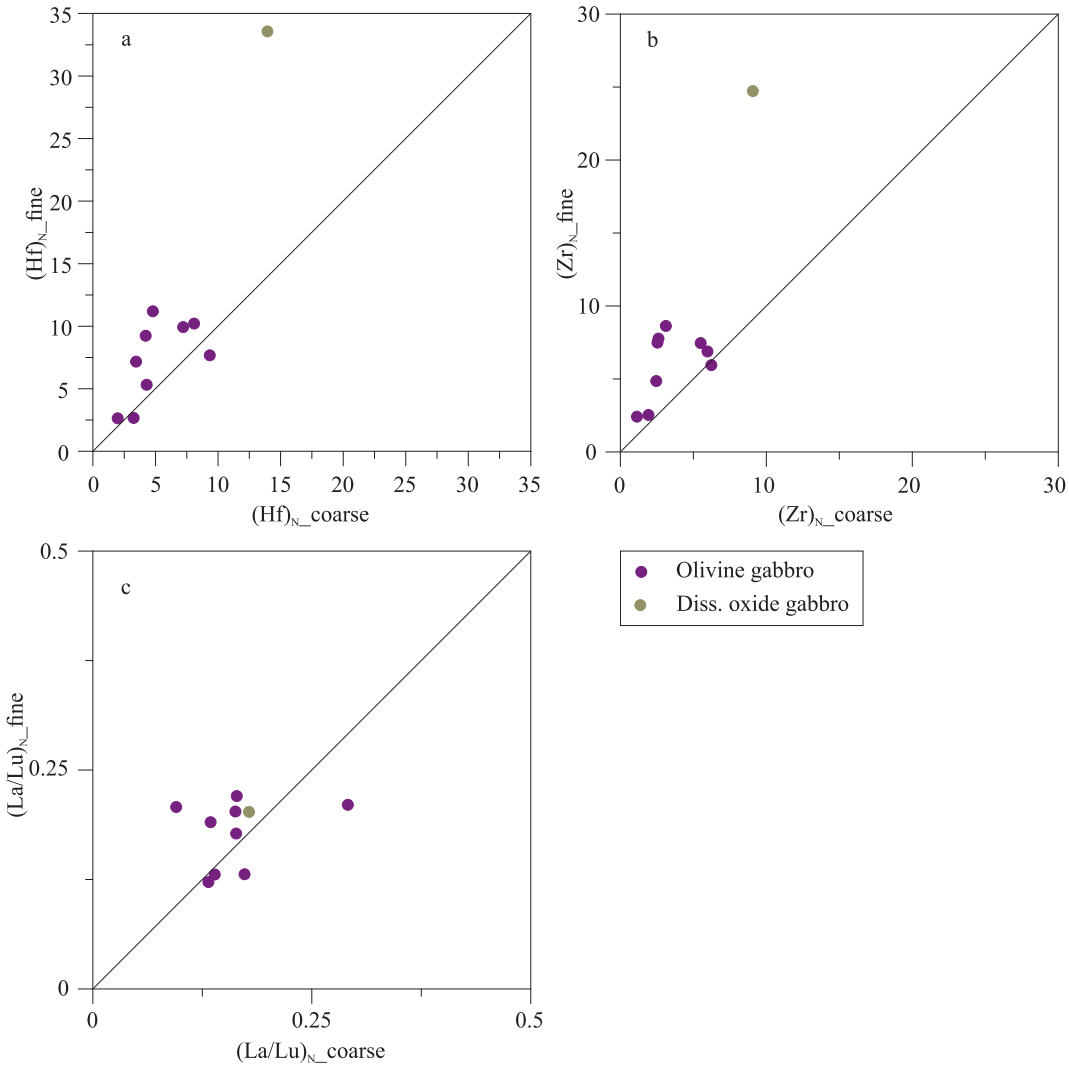

Fig. 17. Correlated incompatible trace element composition of clinopyroxene between the coarser and finer layers. a. Hf, b. Zr. The finer layers are consistently enriched in these elements. c. variation of trace element fractionation across the two domains. $(La/Lu)_N$ have higher values in the finer horizons.

gest dissolution of olivine by a melt that was precipitating clinopyroxene concurrently. Plagioclase embayed against olivine (Fig. 4b) reflects a disequilibrium texture, where crystallization of olivine took place at the expense of plagioclase. Similarly, Fig. 4e shows embayment of clinopyroxene against irregular shaped olivine, which indicates disequilibrium of these phases with the invading melt. Occurrence of olivine as interstitial phase between plagioclase grains in finer olivine gabbro (Fig. 4f) suggests precipitation of olivine. Orthopyroxene also locally develops as interstitial phase between olivine and plagioclase (Fig. 4g, h) in both coarse- and fine-grained lithologies. This and other disequilibrium textures together suggest synchronous dissolution-precipitation of olivine, plagioclase and clinopyroxene. Nonetheless, plagioclase grains often show deformation twinning (Fig. 4a, c), which suggest compaction driven deformation within a cumulate pile (Holness et al., 2017; Meurer and Boudreau, 1998, Ferrando et al., 2021b). However, none of the above-mentioned textures are compatible with the interaction between cumulate pile and oxide-rich melts. Thus, it is likely that the olivine gabbros resulted from the interaction with relatively primitive melt, which did not undergo much fractionation.

Oxide-bearing rocks on the other hand, display textures indicating interaction with both oxide-undersaturated primitive melt and oxide rich melt. Plagioclase grains with planar to resorbed contacts are embayed in clinopyroxene oikocrysts (Fig. 5a, b). Locally, large olivine grains enclose plagioclase chadacrysts with resorbed contacts ((Fig. 5b). Large clinopyroxene oikocrysts enclose corroded olivine at places. These textures are consistent with those recorded from olivine gabbros. These textural features in oxide-bearing rocks are complemented by textures associated with evolved phases like amphibole and/or Fe-Ti oxide. For instance, the lobate rims of olivine + clinopyroxene in Fig. 5c indicates the dissolution of these minerals by Fe-Ti rich melt. Irregular shaped, resorbed islands of plagioclase and amphibole in Fe-Ti oxide (Fig. 5d) indicate interaction with oxide saturated melt. Orthopyroxene is also corroded against Fe-Ti oxide at places (Fig. 5d), which indicate dissolution of evolved phases like orthopyroxene, amphibole by oxide-rich melt. Such textures are also ubiquitous in the finer horizons of oxide-bearing lithologies. Fig. 5e shows corroded plagioclase, clinopyroxene and orthopyroxene by Fe-Ti rich melt, which reflect that this melt percolated through the finer horizons modifying their textural characteristics. During fractionation of MORB, ilmenite, magnetite/titanomagnetite appear relatively late on the liquidus; usually at ~ 4 wt% MgO, below 1100 °C (MacLeod et al., 2017; Botcharnikov et al., 2008; Koepke et al., 2018). Compaction in the cumulate pile during the formation of olivine gabbro

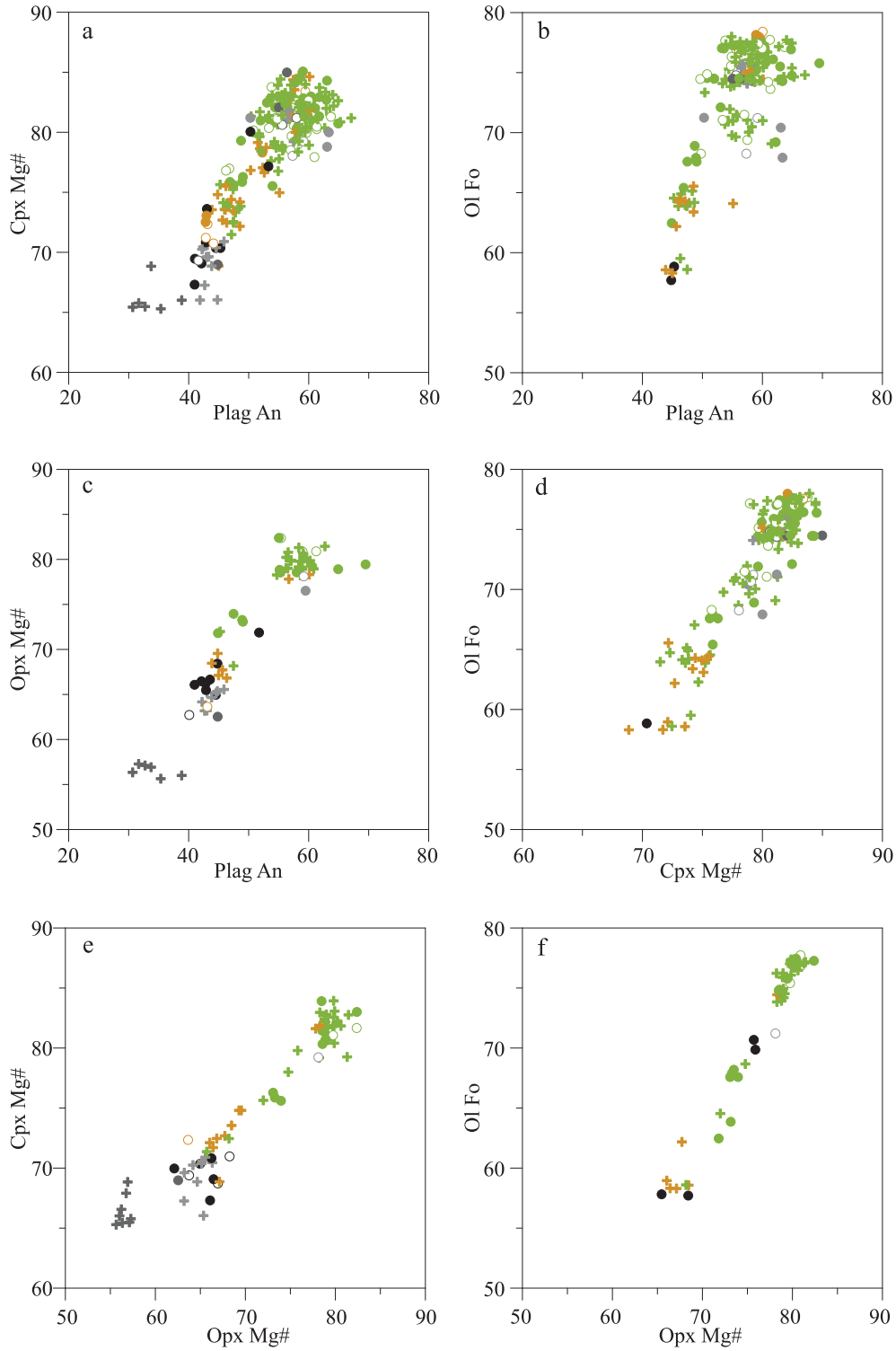

Fig. 18. Covariation plots of anorthite content (100* cationic Ca/ [Ca + Na + K]) of plagioclase (Plag) and Mg# (100* cationic Mg/[Mg + Fe]; all Fe is considered as Fe^{2+}) of clinopyroxene (Cpx), olivine (Ol), and orthopyroxene (Opx) from Hole U1473A rocks. Grains proximal to each other have been selected and paired for this plot. Notable correlations observed from these plots indicate chemical equilibrium among these minerals. Symbols are same as in Fig. 6. Plag = plagioclase, Cpx = clinopyroxene, Ol = olivine, Fo = forsterite content, An = anorthite content.

squeezed out majority of the intercumulus melts. These intercumulus melts are evolved in nature, with high oxide- and water-saturation. Here we propose that, interaction of these evolved melts with U1473A gabbro pile resulted in the formation of oxide-gabbros. Thus, considering all the textual features recorded in Hole U1473A gabbros, it is evident that the oxide-gabbros (sensu lato) were developed by multiple phases of melt-rock interaction.

6.2.2.2. Geochemical evidences. Several authors have proposed that the lower oceanic gabbros in Atlantis Bank have undergone reactive porous flow to certain extents (e.g.- Gao et al., 2007;

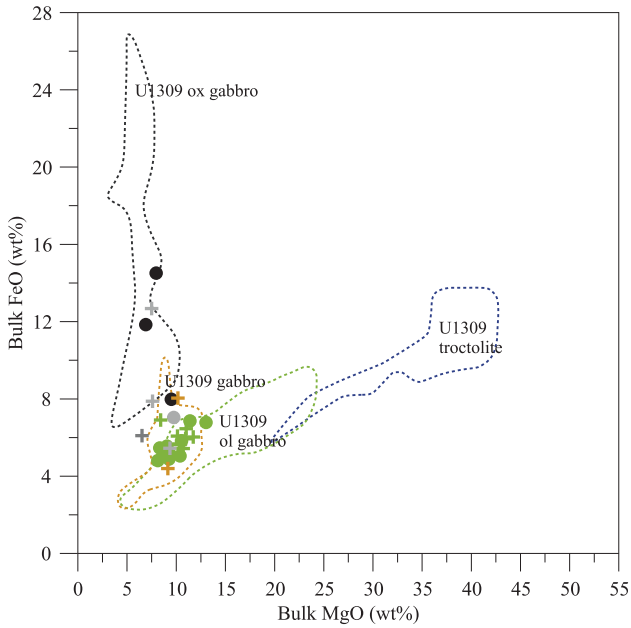

Fig. 19. MgO vs FeO (total) variation of U1473A gabbros. Fields of U1309D [modified from Godard et al. (2009)] rocks are shown for comparison and to highlight the reaction pathway between the primitive cumulates and intercumulus melt forming relatively evolved lithologies.

Lissenberg and MacLeod, 2016; MacLeod et al., 2017; Dick et al., 2019a; 2019b; Sanfilippo et al., 2020; Zhang et al., 2020; Boulanger et al., 2020, 2021; Ferrando et al., 2021a, b).

Clinopyroxenes with high Mg#s are ubiquitously recorded from Atlantis Bank (e.g., Boulanger et al., 2020), however, some of them are characterized by high TiO_2 content (Fig. 7d). Such high Ti, high Mg# clinopyroxenes are commonly recorded from other oceanic ridges as well (e.g.- Hess Deep, Lissenberg et al. (2013) and Kane Megamullion at MAR, Lissenberg and Dick (2008)) and interpreted to be interstitial in nature. Hole U1473A clinopyroxenes have TiO_2 content extending up to 1.4 wt%, suggesting that they were crystallized from evolved melts with TiO_2 content as high as 3.68 wt% (using 0.38 as partition coefficient between clinopyroxene and melt, taken from Hart and Dunn, 1993). To achieve such high TiO_2 content, the equilibrium melt has to undergo extensive fractionation, which would lower the clinopyroxene Mg# considerably. However, some of the high TiO_2 clinopyroxenes are characterised by significantly high Mg# (up to ~ 83) (Fig. 7d) and thus cannot be explained by simple fractionation process. After fractionating the primitive cumulate phases, the interstitial melts become relatively rich in Ti and migrate through the cumulate pile. Interaction of these Ti-rich melts with the early formed olivines in the crystal matrix while remained entrapped in the troctolites, led to their high Mg# (Lissenberg and Dick. 2008). Chakraborty (1997) experimentally deduced the rapid interdiffusion of Fe-Mg between olivine and melt, which corroborates with the above-mentioned process where interstitial clinopyroxenes acquire their high Mg# from the primitive olivine crystals.

Despite the fair correlations, there is a significant range (~10 mol% or greater sometime) in plagioclase An content at any particular Mg# for clinopyroxene and olivine (Fig. 18a, b). Only orthopyroxene shows a significantly tighter correlation (Fig. 18c) (Supplemental Table S10), which probably reflects the ease of oli-

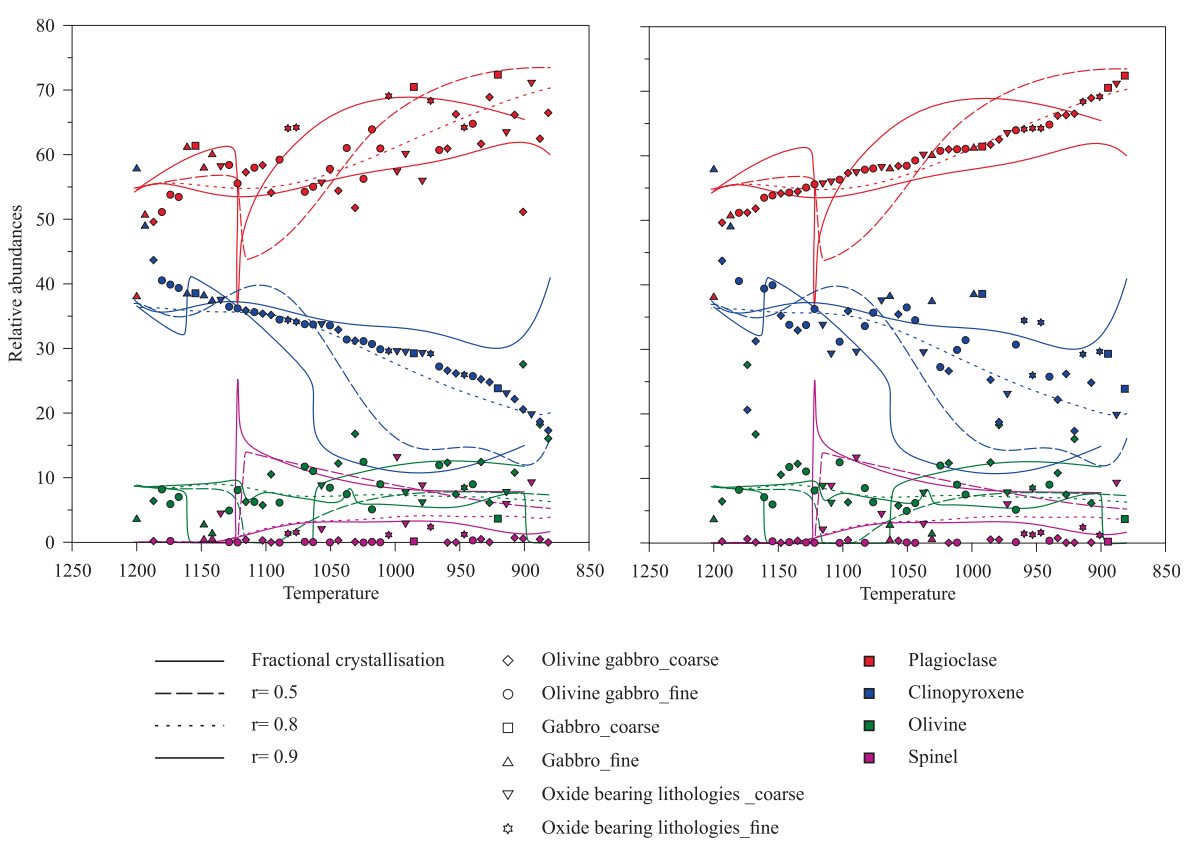

Fig. 20. Relation between the modal abundances of different phases in the studied samples and modal abundances obtained from the AFC modelling arranged with respect to temperature. Abundances of clinopyroxene decrease, and that of plagioclase increase with progressive fractional crystallization. Following this principle, modal abundances of clinopyroxene and plagioclase have been arranged along decreasing temperature, and have been correlated to the calculated AFC curves. a. Highest concentration of clinopyroxene and b. lowest concentration of plagioclase have been assigned to the starting temperature of our model (~1200° C). Modal abundances of plagioclase in a. and clinopyroxene in b. is plotted between the AFC curves of r = 0.8 and 0.9. Olivine and spinel abundances is also plotted and scattered between r values of 0.8 and 0.9.

vine re-equilibration (Dick et al., 2002). Also, mafic silicates show significant scatter in these covariation diagrams (Fig. 18d, e). Various processes can be accounted for this scattering, viz. (i) intrusion and crystallization of a range of basaltic melts owing to different degrees of mantle melting (Meyer et al., 1989), (ii) large variations in mantle potential temperature or mantle source composition (Dick et al., 2019a), or (iii) post-cumulus re-equilibration of the crystal mush with the interstitial melt (Meyer et al., 1989, Dick et al., 2002). Significant range of Ca# at constant Mg# recorded from the whole rock data (Fig. 14a), which is also consistent with the finding from Atlantis II Fracture Zone (Dick et al., 1991b) can explain the scatter noted in Fig. 18. However, this cannot explain the large scatter of clinopyroxene TiO_2 at a particular clinopyroxene Mg# (Fig. 7d) or range of Ni for any particular Fo content in olivine in Fig. 12a. Also, scattering to such an extent in the adjacent grains due to differences in mantle potential temperature and/or mantle source composition does not seem to be a viable explanation. Alternatively, such distribution of data can be attributed to incomplete post-cumulus re-equilibration of the crystal mush with the permeable intercumulus melt (Meyer et al., 1989; Dick et al., 2002). Nevertheless, higher concentration of data towards high An end is noteworthy (Fig. 18a, b, c). This is perhaps due to buoyancy of plagioclase in basaltic melt and it is less susceptible to diffusion compared to olivine (Meyer et al., 1989).

In describing melt-rock interaction for Atlantis Massif, Godard et al. (2009) demonstrated two mutually perpendicular trends in FeO-MgO whole rock wt% plot (Fig. 19) that delineate the reaction pathways between primitive melt and peridotite, resulting in troctolite formation, and evolved melt and gabbro to produce oxide gabbro (sensu lato) respectively. However, the trend here in Atlantis Bank follows the later, suggesting hybridization of olivine gabbro by percolating evolved melts. This line of evidence also explains the formation of oxide-gabbro (sensu lato) by interaction between relatively evolved Fe-Ti rich melt and gabbro and/or olivine gabbro, not by pure fractional crystallization. On the contrary, the origin of oxide gabbros (sensu lato) in oceanic settings is not always explained by a reactive process. For example, Natland et al. (1991) hypothesized progressive iron enrichment to the point of immiscible separation of a dense, iron-rich liquid from which oxide-rich concentrates form.

6.3. Assimilation and fractional crystallization

Assimilation-fractional crystallization (AFC) has been advocated as an effective and relatively realistic way to facilitate melt-rock reaction via reactive porous flow (Meyer et al., 1989; Coogan et al., 2000; Dick et al., 2002; Ridley et al., 2006; Gao et al., 2007; Lissenberg et al., 2013; Lissenberg and MacLeod, 2016; Sanfilippo

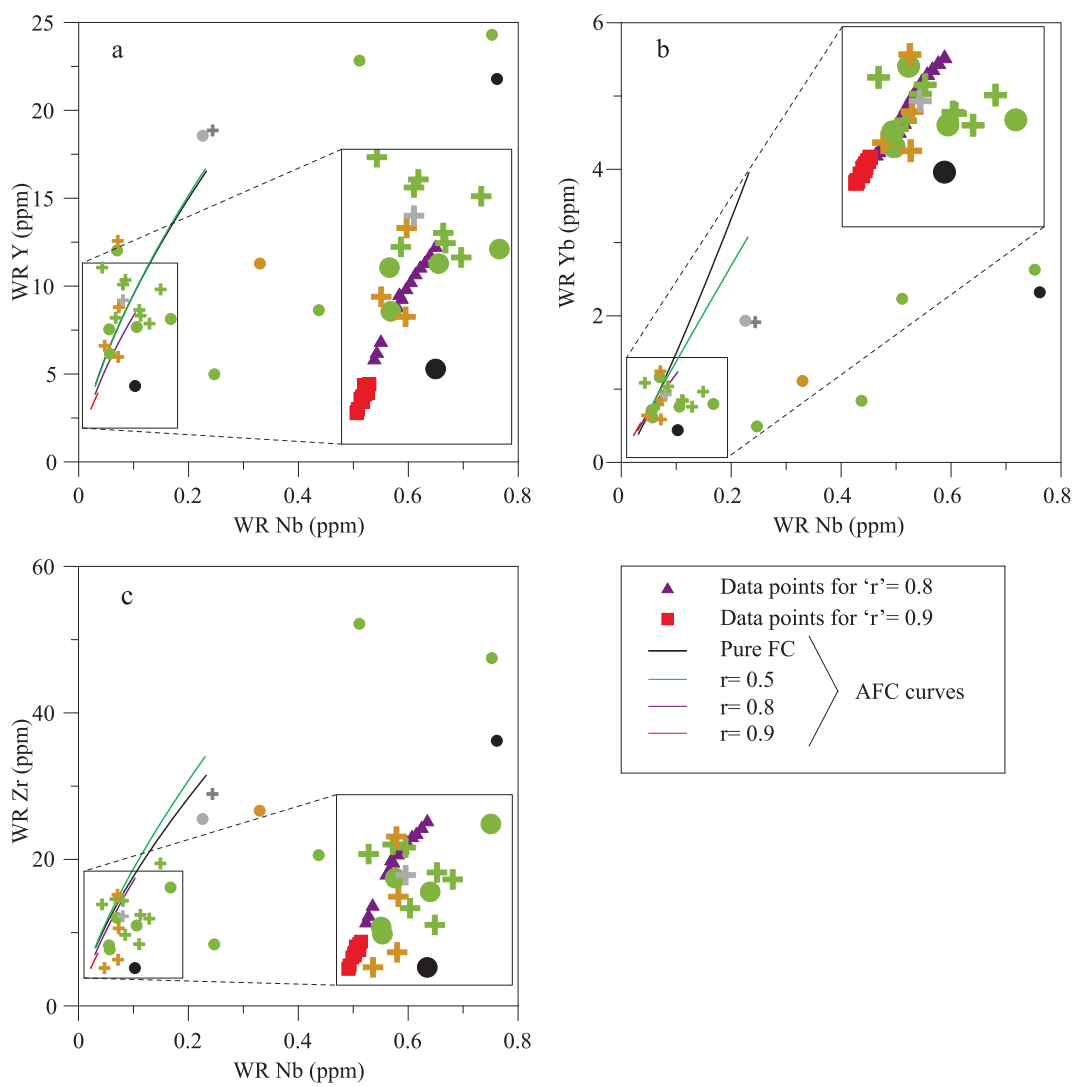

Fig. 21. Trace element variations in U1473A gabbros (sensu lato). AFC curves are calculated for different 'r' values and pure fractional crystallization (FC) curves are also shown for comparison.

et al., 2015, 2020; Boulanger et al., 2020, 2021; Ferrando et al., 2021a). This model assumes a percolating melt through lower oceanic crustal reservoir assimilating the infiltrated crystal mush and simultaneously fractionating solid minerals. Recent works (Zhang et al., 2020; Ferrando et al. 2021a, Sanfilippo et al., 2020; Boulanger et al., 2021) pointed out AFC as the key mechanism to explain the lithological, geochemical diversity for Hole U1473A.

To explore the extent of melt-rock reaction in Atlantis Bank we have developed thermodynamic AFC models in an attempt to replicate the lithological and compositional variability of Hole U1473A (specifically for the bottommost geochemical cycle) at different assimilation (M_a)/ fractionation (M_c) ratios ($r = M_a/M_c$) over a range of temperature using alphaMELTS (Smith and Asimow, 2005; Ghiorso and Sack, 1995). To perform AFC modelling, we first need to estimate the parental melt for this particular set of lithologies. Niu et al. (2002) estimated that the lithologies of Hole 735B were crystallized from a melt having Mg# $\leq$ ~63.7, which we consider as a good approximation for Hole U1473A in view of its proximity to Hole 735B. In order to reconstruct the parent melt composition, we looked into the MORB compositions from SWIR. Since the mantle beneath SWIR is heterogeneous as pointed out by Meyzen et al. (2003), we have taken the MORB data with highest Mg# from 'Zone B' (Meyzen et al., 2003) as the representative of SWIR MORB (Sample no.- DR46- 1–6; Mg# = 63) (Supplemental Table S11). Though this Mg# is very close to the estimated parental melt of Niu et al. (2002), in order to make our modelling consistent we have not directly used this composition, rather first tried to trace back the potential primary melt composition (PM_DR46- 1–6 in Supplemental Table S11) of SWIR MORB using PRIMACALC2 (Kimura and Ariskin, 2014). This primary melt is by definition different from the parental magma because it has its origin in the earth's mantle by partial melting and supposedly has not undergone any modification by any of the differentiation processes. Our result yields Mg# value of 77.4 for the primary melt which is expectedly substantially higher than the melt (Mg#$\leq$ ~63.7) parental to Hole 735B as well as for Hole U1473A. At slow-spreading ridges, due to slow upwelling of mantle a significant amount of heat is lost by conduction (Bown and White, 1994; Niu et al., 2002) leading to thick, cold thermal boundary layer above the mantle (Niu and Hékinian, 1997; Niu, 1997). Therefore, it is anticipated that the primary magma (Mg# = 77.4) must have crystallized out the primitive cumulates (forsteritic olivine, anorthitic plagioclase, chromite) by enroute fractionation as suggested by Niu (1997) and Niu et al. (1997). In order to constrain a melt with Mg# < 63.7, we fractionated the primary melt (PM_DR46- 1–6, Mg# = 77.4) using alphaMELTS software package (Smith and Asimow, 2005) of MELTS algorithm (Ghiorso and Sack, 1995) and conceived this melt as parental to Hole U1473A lithologies (Supplemental Table S11). The software predicts the temperature of the melt to be ~ 1200 °C which is very close to the liquidus of clinopyroxene. Subsequently we have continued to fractionate the parental magma and the fractionated product obtained after each calculation has been taken as the assimilant, and mixed in varying proportions based on different 'r' values in the next phase of calculation. This process has been run iteratively at temperature interval of ~ 20 °C. We usually stopped our experiment usually at 880 °C where it grossly matches with the whole rock composition especially in higher 'r" values.

Previous studies dealing with numerical AFC models (e.g., Zhang et al., 2020; Ferrando et al. 2021a, Sanfilippo et al., 2020) focuses only into replicating the mineral chemistry. The methodology used in this study however allows us to specifically looked into mineralogical evolution in terms of chemical as well as modal

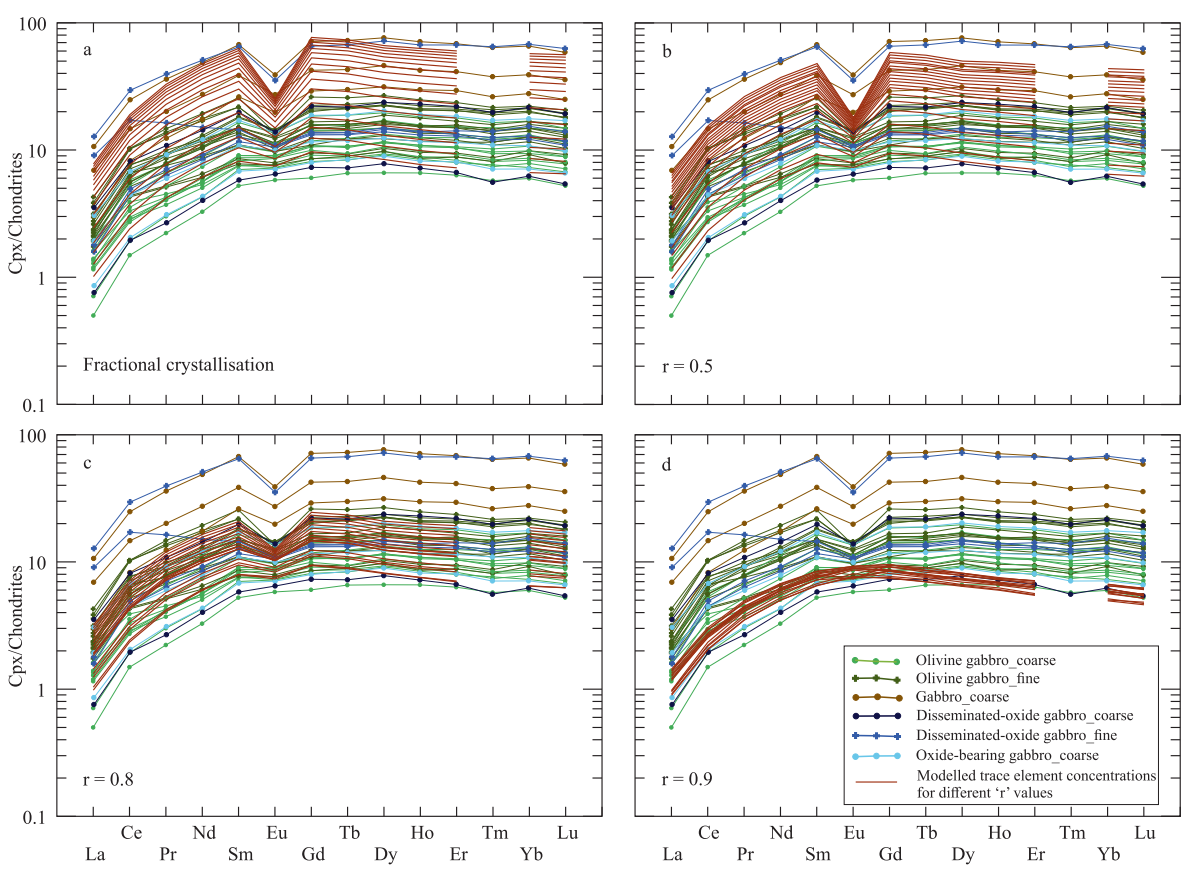

Fig. 22. Comparison of clinopyroxene REE compositions of the studied samples to the REE compositions of the modelled clinopyroxenes for a. pure fractional crystallization, b. r = 0.5, c. r = 0.8, (d) r = 0.9. Notable resemblance is observed for r = 0.8.

assemblages. Here, we have adopted a novel approach of matching the modal composition predicted from this calculation (for different 'r' values) with that actually existing in the recovered rocks, corresponding to their temperature of formation. Generally, during progressive fractional crystallization with temperature-reduction clinopyroxene content tends to decrease which is compensated by plagioclase formation. This behaviour is found in our AFC modelling too, further justifying our experimental procedure. This along with the liquidus temperature of clinopyroxene, led us to assume sample with highest concentration of clinopyroxene would have been formed very near to starting temperature (~1200 °C) of our model. Then considering the general tendency of clinopyroxene reduction, the modal clinopyroxenes of the Hole U1473A lithologies have been sorted in decreasing order in the temperature interval obtained from AFC calculations. This fixes the modal proportion of other mineral phases (viz. plagioclase, olivine and spinel) of a particular lithology corresponding to its assigned temperature (Fig. 20a). The same exercise has been repeated while sorting the modal plagioclase content in increasing order (Fig. 20b).

Fig. 20 shows the relative mineralogical abundance predicted by the AFC model for different r values (0-pure fractional crystallization, 0.5, 0.8, 0.9) (Supplemental Table S12). This allows us to directly compare the results of the models with the observed modal assemblages of the studied rocks. Fig. 20a depicts that the actual clinopyroxene modal do not match with the pure fractional crystallization (FC, r = 0) curve and for r = 0.5, rather the abundances have a better match with the modal abundances curve for r = 0.8, and to some context for r = 0.9. Observed modal abundances of the other constituting mineral phases do not abruptly plot with respect to the modelling values supporting the experimental constraints and assumptions of the model. In Fig. 20b plagioclase content is sorted in increasing order with respect to the similar range of temperature, a similar best fit with respect to curve for r = 0.8 (and to some extent for 0.9) is seen. This result provides clinching evidences of significant dependence of modal abundance of the lower crustal rocks on the assimilation (M_a)/fractionation (M_c) ratios ($r = M_a/M_c$).

While considering the whole rock geochemistry, although the curves for different r values show grossly similar trend, the geochemical diversity strongly decreases with higher r values (Fig. 21). The strongest data dispersion is documented for pure fractional crystallization, whereas for r = 0.8–0.9, AFC data cluster around a very narrow range (see insets of Fig. 21). This documentation bears significance because the actual whole rock analytical data display a limited range, scattered mostly around the curves for higher r values. Nonetheless, the computed AFC curves do not show great match with the measured whole-rock data, particularly Nb in the studied samples. This likely owes to the local enrichment of late magmatic phases viz. Fe-Ti oxides and/or brown amphiboles.

Whole-rock compositional variations in the oceanic gabbros are results of several processes; starting from fractional crystallization, reactive porous flow, melt extraction, late melt impregnation to high- and low-temperature alterations. Incorporating all these mechanisms into a single model can be tricky. To discard the effects of crystal-melt separation and alteration, we have compared the REE (Fig. 22) and trace element (Fig. 23) compositional variations of Atlantis Bank clinopyroxenes with that of the modelled clinopyroxene data for different r values. Data spread for r = 0.8 (Fig. 22c, 23c) shows remarkable resemblance to that of the studied samples. This observation corroborates with the

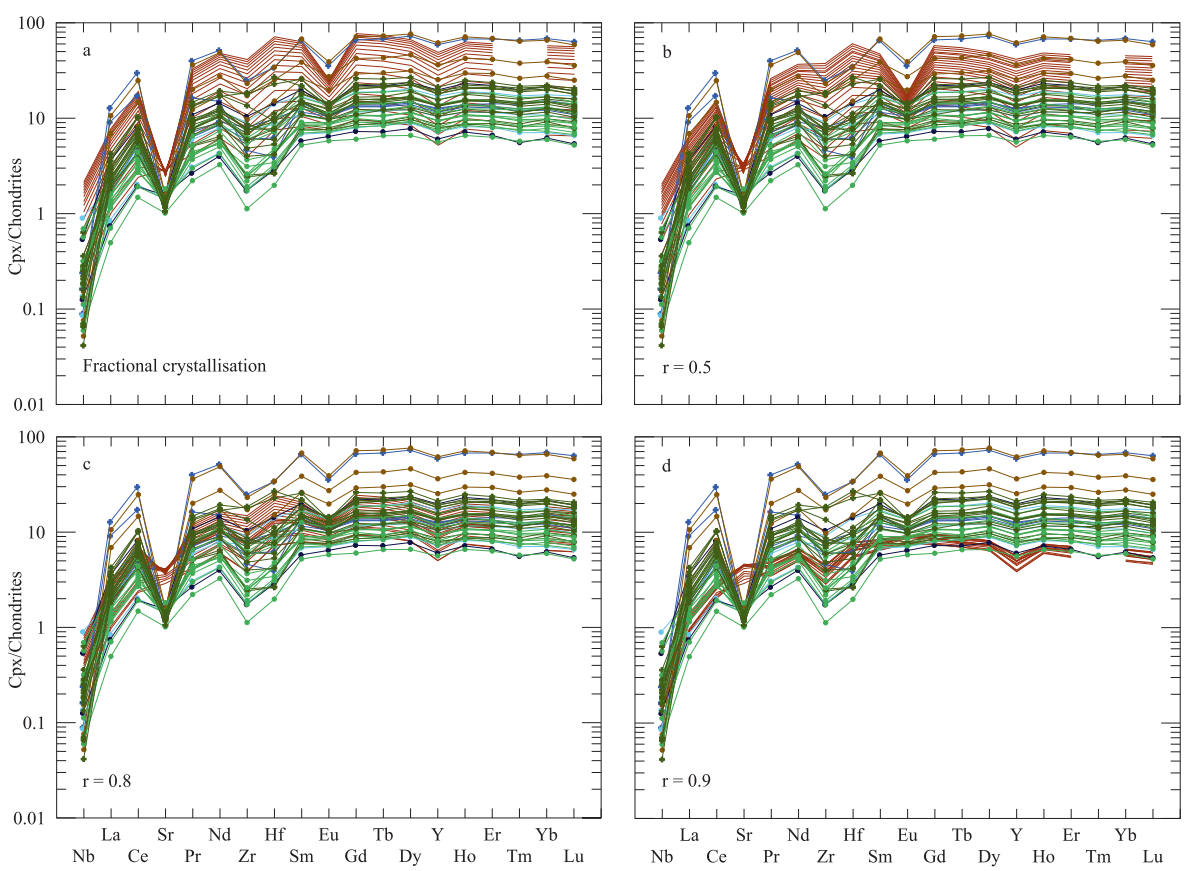

Fig. 23. Comparison of clinopyroxene trace element compositions of the studied samples to that of the modelled clinopyroxenes for a. pure fractional crystallization, b. r = 0.5, c. r = 0.8, d. r = 0.9. Remarkable similarity is noted for r = 0.8, which affirms to the extent of melt-rock interaction. Symbols are same as in Fig. 22.

previous estimations from several other studies (Zhang et al., 2020; Ferrando et al. 2021a, Sanfilippo et al., 2020; Boulanger et al., 2020).

7. Conclusion

Here we report a detailed petrography and geochemical study of the lower crustal gabbroic rocks recovered from the Hole U1473A in Atlantis Bank OCC at ultraslow-spreading Southwest Indian Ridge to shed lights on the tectono-magmatic history of the ridge, aiming to enhance our understanding on the lithospheric architecture of the slow- to ultraslow-spreading ridges as a whole.

Most of the earlier studies are focused only on a particular lithology (for example, olivine gabbro), however, in this study we probed into the complete spectrum ranging from relatively primitive olivine gabbro to evolved oxide-gabbro and documented ubiquitous presence of grain-size layering (with sharp interface) within

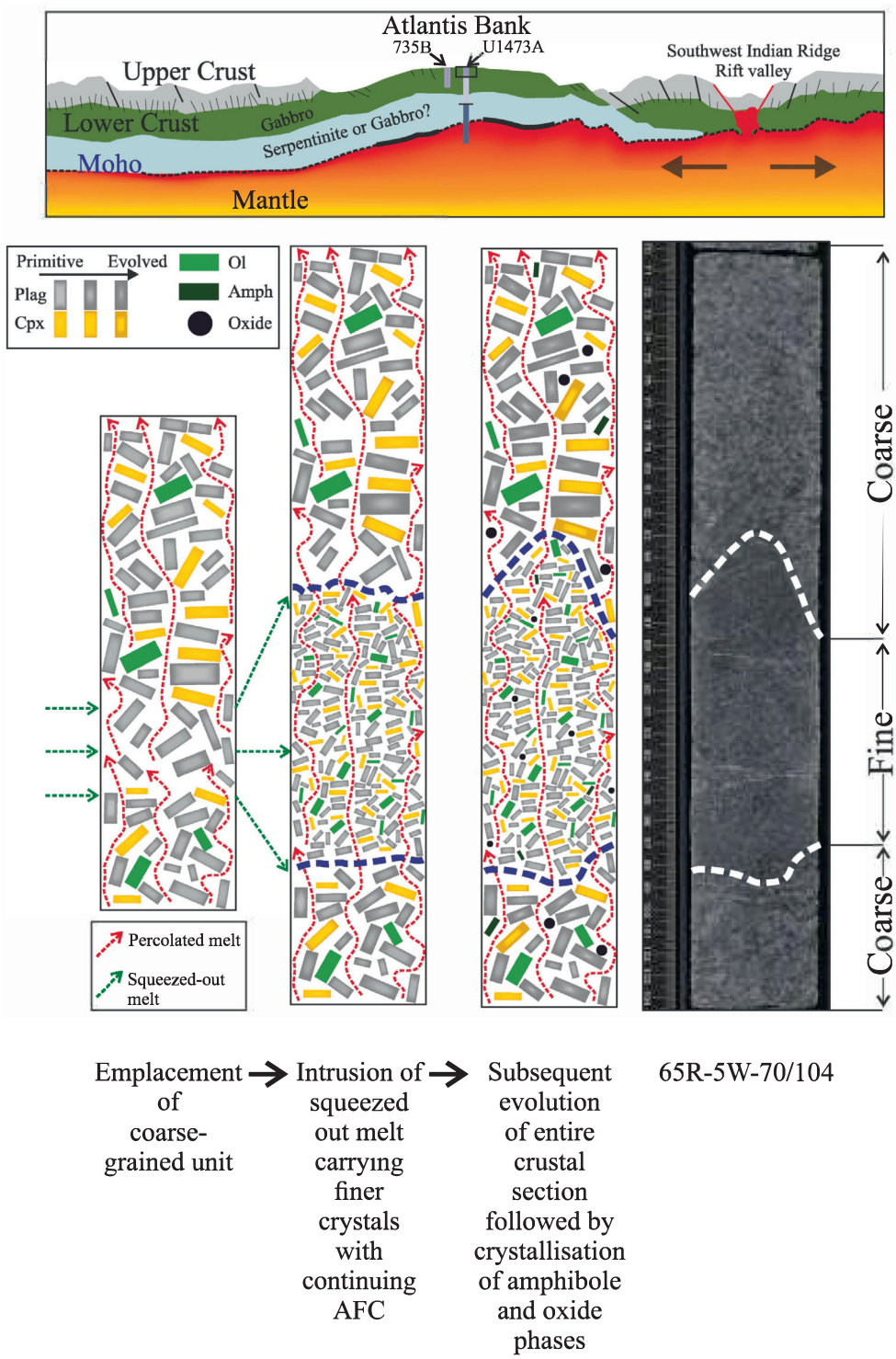

Fig. 24. Schematic diagram illustrating the textural and chemical evolution of the lower oceanic crustal section at Atlantis Bank OCC. Development of grain-size layering is demonstrated and compared with a core section recovered from U1473A.

the lithotypes. This feature has been also reported from the earlier drillings from Atlantis Bank (Hole 735B and Hole 1105A). From detailed geochemical record we found such grain-size variation is accompanied by geochemical changes between the coarser and finer intervals. The finer layers were likely crystallized from the melt squeezed out by compaction or filter pressing within solidifying crystal mush. The compositional comparability between the rims of the coarse-grained crystals and the fine-grained crystals indicates that the melt forming the fine-grained domains was not exotic, rather it was extracted from the adjacent coarse-grained mush and then segregated into fine-grained intervals.

Previous studies dealing with AFC modelling are mostly intensive to mineral chemistry and not the whole rock analysis. Here we use the forward AFC modelling to predict the possible whole rock geochemical behaviour and clinopyroxene trace element data, and compared them with our obtained composition. AFC modelling predicts a geochemical evolutionary trend (diversity) in fractional crystallization (r = 0) which gradually disappears at higher r values; for r = 0.8–0.9 we documented a very restricted range of geochemistry. In our whole rock results from all the studied lithotypes, we observed a similar narrow range which was not previously reported. This provides clinching evidence in support of AFC-influenced crust formation, particularly at high assimilation/fractionation ratio, demonstrating the whole rock geochemical as well as mineral chemical behaviour in such mechanism.

From the petrographic perspective it is quite evident that the lower crustal lithotype variability is *sensu-stricto* controlled by the modal mineral assemblages. However, role of AFC in controlling such modal assemblage (eventually gives rise to the architecture) has not been discussed much earlier. The robust sampling strategy and the new modelling approach of this study allowed us to directly look into the progressive change in the modal proportion with respect to the variable AFC conditions. With certain number of reasonable assumptions, we have been able to replicate the observed modal assemblages for high r values (0.8–0.9) as predicted from the earlier studies.

From our comprehensive collation and synthesis, we here present a schematic model (Fig. 24) of crust (lower) formation for the Atlantis Bank. It starts with an initial emplacement of a crystal mush consisting only of coarser materials. Reactive melt percolating through the cumulate pile continuously keeps on changing the composition of the constituting phases. Melts from the coarser horizons are then extracted owing to compaction, and squeezed out of the crystal mush. The crystallizing product of this melt cannot grow larger due to absence of any incipient crystals in this melt, hence requiring longer times to nucleate a crystal. Finally, smaller crystals develop, which maintain compositional resemblance with the rims of the formerly grown coarser zoned crystals owing to continuous reactive porous flow throughout the crustal section.

Declaration of Competing Interest

The authors declare that they have no known competing financial interests or personal relationships that could have appeared to influence the work reported in this paper.

Acknowledgements

This study uses samples provided by the International Ocean Discovery Program (IODP) (https://www.iodp.org/about-iodp). The authors acknowledge the captain, the crew, and the staff of the JOIDES Resolution for their support during Expedition 360. BG thankfully acknowledges the Science Party for all technical discussions during the cruise. We thank the anonymous reviewers, and associate editor Zeming Zhang for their constructive comments that helped to improve this paper. This research was supported by grants received from the National Centre for Polar and Ocean Research, Government of India (No. NCAOR/IODP/2017/9).

AD, BG and TM designed research; BG, TM, LF participated in the science expedition (IODP 360); BG, TM, AT, DKN collected and interpreted data; AD, BG, DB wrote the manuscript; AD, DB, MB, MK, SR, SC drafted figures. All authors read, commented on the original manuscript and also took part in the revision. They all approved the manuscript and agreed to its submission.

Appendix A. Supplementary material

Supplementary data to this article can be found online at https://doi.org/10.1016/j.gr.2022.08.008.

References

Baines, A.G., Cheadle, M.J., Dick, H.J.B., Hosford Scheirer, A., John, B.E., Kusznir, N.J., Matsumoto, T., 2003. Mechanism for generating the anomalous uplift of oceanic core complexes: Atlantis Bank, Southwest Indian Ridge. Geology 31, 1105–1108. https://doi.org/10.1130/G19829.1.

Barriere, M., 1981. On curved laminae, graded layers, convection currents and dynamic crystal sorting in the Ploumanac'h (Brittany) subalkaline granite. Contrib. Miner. Petrol. 77, 214–224. https://doi.org/10.1007/BF00373537.

Bédard, J., 2010. Parameterization of the Fe–Mg exchange coefficient (Kd) between clinopyroxene and silicate melts. Chem. Geol. 274, 169–176. https://doi.org/10.1016/j.chemgeo.2010.04.003.

Blackman, D.K., 2006 and the Expedition 304/305 Scientists, 2006. Proceedings of the Integrated Ocean Drilling Program, 304/305: College Station, TX (Integrated Ocean Drilling Program Management International, Inc.). http://dx.doi.org/10.2204/iodp.sp.304305.2004.

Blackman, D.K., Collins, J.A., 2010. Lower crustal variability and the crust/mantle transition at the Atlantis Massif oceanic core complex. Geophys. Res. Lett. 37. https://doi.org/10.1029/2010GL045165.

Bloomer, S.H., Meyer, P.S., Dick, H.J.B., Ozawa, K., Natland, J.H., 1991. Textural and mineralogic variations in gabbroic rocks from Hole 735B. In: Von Herzen, R., Robinson, P.T., et al., Proceedings of the Ocean Drilling Program, Scientific Result, 118. College Station, TX (Ocean Drilling Program), pp. 21–39. doi:10.2973/odp.proc.sr.118.136.1991.

Botcharnikov, R.E., Almeev, R.R., Koepke, J., Holtz, F., 2008. Phase Relations and Liquid Lines of Descent in Hydrous Ferrobasalt—Implications for the Skaergaard Intrusion and Columbia River Flood Basalts. J. Petrol. 49, 1687–1727. https://doi.org/10.1093/petrology/egn043.

Boulanger, M., France, L., Deans, J.R.L., Ferrando, C., Lissenberg, C.J., Handt, A., 2020. Magma Reservoir Formation and Evolution at a Slow-Spreading Center (Atlantis Bank, Southwest Indian Ridge). Front. Earth Sci. 8. https://doi.org/10.3389/feart.2020.554598.

Boulanger, M., 2020. The fate of melts within the slow-spreading lower oceanic crust: New insights from Atlantis Bank (Southwest Indian Ridge). Earth Sciences. Ph.D. Thesis at Université de Lorraine.

Boulanger, M., France, L., Ferrando, C., Ildefenso, B., Ghosh, B., Sanfilippo, A., Liu, C-Z., Morishita, T., Koepke, J., Bruguier, O., 2021. Magma-Mush Interactions in the Lower Oceanic crust: Insights from Atlantis Bank Layered Series (Southwest Indian Ridge). J. Geophys. Res.: Solid Earth 126, p.e2021JB022331. https://doi.org/10.1029/2021JB022331.

Bown, J.W., White, R.S., 1994. Variation with spreading rate of oceanic crustal thickness and geochemistry. Earth Planet. Sci. Lett. 121, 435–449. https://doi.org/10.1016/0012-821X(94)90082-5.

Brandeis, G., Jaupart, C., Allègre, C.J., 1984. Nucleation, crystal growth and the thermal regime of cooling magmas. J. Geophys. Res.: Solid Earth 89, 10161–10177. https://doi.org/10.1029/JB089iB12p10161.

Brunelli, D., Sanfilippo, A., Bonatti, E., Skolotnev, S., Escartin, J., Ligi, M., Ballabio, G., Cipriani, A., 2020. Origin of oceanic ferrodiorites by injection of nelsonitic melts in gabbros at the Vema Lithospheric Section. Mid Atlantic Ridge. Lithos 368–369. https://doi.org/10.1016/j.lithos.2020.105589.

Buck, W.R., Lavier, L.L., Poliakov, A.N.B., 2005. Modes of faulting at mid-ocean ridges. Nature 434, 719–723. https://doi.org/10.1038/nature03358.

Canales, J.P., Dunn, R.A., Arai, R., Sohn, R.A., 2017. Seismic imaging of magma sills beneath an ultramafic-hosted hydrothermal system. Geology 45, 451–454. https://doi.org/10.1130/G38795.1.

Cann, J.R., Blackman, D.K., Smith, D.K., McAllister, E., Janssen, B., Mello, S., Avgerinos, E., Pascoe, A.R., Escartin, J., 1997. Corrugated slip surfaces formed at ridge–transform intersections on the Mid-Atlantic Ridge. Nature 385, 329–332. https://doi.org/10.1038/385329a0.

Cannat, M., 1993. Emplacement of mantle rocks in the seafloor at mid-ocean ridges. J. Geophys. Res.: Solid Earth 98, 4163–4172. https://doi.org/10.1029/92JB02221.

Cannat, M., Sauter, D., Mendel, V., Ruellan, E., Okino, K., Escartin, J., Combier, V., Baala, M., 2006. Modes of seafloor generation at a melt-poor ultraslow-spreading ridge. Geology 34, 605–608. https://doi.org/10.1130/G22486.1.

Chakraborty, S., 1997. Rates and mechanisms of Fe–Mg interdiffusion in olivine at 980°–1300°C. J. Geophys. Res.: Solid Earth 102, 12317–12331. https://doi.org/10.1029/97JB00208.
Chen, C.F., Turner, J.S., 1980. Crystallisation in a double-diffusive system. J. Geophys. Res. 85, 2573–2593. https://doi.org/10.1029/JB085iB05p02573.
Collier, M.L., Kelemen, P.B., 2010. The case for reactive crystallization at mid-ocean ridges. J. Petrol. 51, 1913–1940. https://doi.org/10.1093/petrology/egq043.
Coogan, L.A., Saunders, A.D., Kempton, P.D., Norry, M.J., 2000. Evidence from oceanic gabbros for porous melt migration within a crystal mush beneath the Mid-Atlantic Ridge. Geochem. Geophys. Geosyst. 1. https://doi.org/10.1029/2000GC000072.
Coogan, L.A., Wilson, R.N., Gillis, K.M., MacLeod, C.J., 2001. Near-solidus evolution of oceanic gabbros: insights from amphibole geochemistry. Geochim. Cosmochim. Acta 65, 4339–4357. https://doi.org/10.1016/S0016-7037(01)00714-1.
Detrick, R.S., Buhl, P., Vera, E., Mutter, J., Orcutt, J., Madsen, J., Brocher, T., 1987. Multi-channel seismic imaging of a crustal magma chamber along the East Pacific Rise. Nature 326, 35–41. https://doi.org/10.1038/326035a0.
Dick, H.J.B., Schouten, H., Meyer, P.S., Gallo, D.G., Bergh, H., Tyce, R., Patriat, P., Johnson, K.T.M., Snow, J., Fisher, A., 1991a. Tectonic evolution of the Atlantis II fracture zone. In Von Herzen, R., Robinson, P.T., et al., Proc. ODP, Sci. Results, 118: College Station, TX (Ocean Drilling Program), 359–398. doi:10.2973/odp.proc.sr.118.156.1991.
Dick, H.J.B., Meyer, P.S., Bloomer, S., Kirby, S., Stakes, D., Mawer, C., 1991b. Lithostratigraphic evolution of an in-situ section of oceanic Layer 3. In: Von Herzen, R.P., Robinson, P.T., et al., Proceedings of the Ocean Drilling Program, Scientific Results, 118. College Station, TX (Ocean Drilling Program), pp. 439–538. doi:10.2973/odp.proc.sr.118.128.1991.
Dick, H.J.B., MacLeod, C.J., Blum, P., Abe, N., Blackman, D.K., Bowles, J.A., Cheadle, M. J., Cho, K., Ciazela, J., Deans, J.R., Edgcomb, V.P., Ferrando, C., France, L., Ghosh, B., Ildefonse, B., John, B., Kendrick, M.A., Koepke, J., Leong, J.A.M., Liu, C., Ma, Q., Morishita, T., Morris, A., Natland, J.H., Nozaka, T., Plumper, O., Sanfilippo, A., Sylvan, J.B., Tivey, M.A., Tribuzio, R., Viegas, G., 2019b. Dynamic accretion beneath a slow-spreading ridge segment: IODP Hole 1473A and the Atlantis Bank Oceanic Core Complex. J. Geophys. Res.: Solid Earth 124, 12631–12659. https://doi.org/10.1029/2018JB016858.
Dick, H.J.B., MacLeod, C.J., Blum, P., Abe, N., Blackman, D.K., Bowles, J.A., Cheadle, M. J., Cho, K., Ciazela, J., Deans, J.R., Edgcomb, V.P., Ferrando, C., France, L., Ghosh, B., Ildefonse, B., John, B., Kendrick, M.A., Koepke, J., Leong, J.A.M., Liu, C., Ma, Q., Morishita, T., Morris, A., Natland, J.H., Nozaka, T., Plumper, O., Sanfilippo, A., Sylvan, J.B., Tivey, M.A., Tribuzio, R., Viegas, G., 2017. Expedition 360 summary. In: Proceedings of the International Discovery Program. IODP, College Station, TX, p. 360. https://doi.org/10.14379/iodp.proc.360.101.2017.
Dick, H.J.B., Kvassnes, A.J., Robinson, P.T., MacLeod, C.J., Kinoshita, H., 2019a. The Atlantis Bank Gabbro Massif, Southwest Indian Ridge. Prog. Earth Planet. Sci. 6, 1–70. https://doi.org/10.1186/s40645-019-0307-9.
Dick, H.J., Natland, J.H., Alt, J.C., Bach, W., Bideau, D., Gee, J.S., Haggas, S., Hertogen, J. G., Hirth, G., Holm, P.M., Ildefonse, B., 2000. A long in situ section of the lower ocean crust: results of ODP Leg 176 drilling at the Southwest Indian Ridge. Earth Planet. Sci. Lett. 179, 31–51. https://doi.org/10.1016/S0012-821X(00)00102-3.
Dick, H.J., Ozawa, K., Meyer, P.S., Niu, Y., Robinson, P.T., Constantin, M., Hebert, R., Maeda, J., Natland, J.H., Hirth, G., Mackie, S., 2002. Primary silicate mineral chemistry of a 1.5-km section of very slow spreading lower ocean crust: ODP hole 735B, Southwest Indian ridge. In: Natland, J.H., Dick H.J.B., Miller, D.J., Von Herzen, R.P., Proceedings of Ocean Drilling Program, Scientific Results, 176. College Station, TX (Ocean Drilling Program), pp. 1-61. https://doi:10.2973/odp.proc.sr.176.001.2002.
Dowty, E., 1980. Crystal growth and nucleation theory and the numerical simulation of igneous crystallization. Phys. Magmat. Processes. 419–486. https://doi.org/10.1515/9781400854493.419.
Engell, J., 1973. A closed system crystal fractionation model for the agpaitic Ilimaussaq intrusion, South Greenland, with special reference to lujavrites. Bull. Geol. Soc. Den. 22, 334–362.
Ferrando, C., France, L., Basch, V., Sanfilippo, A., Tribuzio, R., Boulanger, M., 2021a. Grain Size Variations Record Segregation of Residual Melts in Slow-Spreading Oceanic Crust (Atlantis Bank, 57°E Southwest Indian Ridge). J. Geophys. Res.: Solid Earth 126. https://doi.org/10.1029/2020JB020997.
Ferrando, C., Basch, V., Ildefonse, B., Deans, J., Sanfilippo, A., Barou, F., France, L., 2021b. Role of compaction in melt extraction and accumulation at a slow spreading center: Microstructures of olivine gabbros from the Atlantis Bank (IODP Hole U1473A, SWIR). Tectonophysics 815,. https://doi.org/10.1016/j.tecto.2021.229001 229001.
France, L., Ildefonse, B., Koepke, J., Bech, F., 2010. A new method to estimate the oxidation state of basaltic series from microprobe analyses. J. Volcanol. Geoth. Res. 189, 340–346. https://doi.org/10.1016/j.jvolgeores.2009.11.023.
Gao, Y., Hoefs, J., Hellebrand, E., von der Handt, A., Snow, J.E., 2007. Trace element zoning in pyroxenes from ODP Hole 735B gabbros: diffusive exchange or synkinematic crystal fractionation? Contrib. Miner. Petrol. 153, 429–442. https://doi.org/10.1007/s00410-006-0158-4.
Ghiorso, M.S., Sack, R.O., 1995. Chemical mass transfer in magmatic processes IV. A revised and internally consistent thermodynamic model for the interpolation and extrapolation of liquid-solid equilibria in magmatic systems at elevated temperatures and pressures. Contrib. Miner. Petrol. 119, 197–212. https://doi.org/10.1007/BF00307281.
Godard, M., Awaji, S., Hansen, H., Hellebrand, E., Brunelli, D., Johnson, K., Yamasaki, T., Maeda, J., Abratis, M., Christie, D., Kato, Y., 2009. Geochemistry of a long in-situ section of intrusive slow-spread oceanic lithosphere: Results from IODP Site U1309 (Atlantis Massif, 30 N Mid-Atlantic-Ridge). Earth Planet. Sci. Lett. 279, 110–122. https://doi.org/10.1016/j.epsl.2008.12.034.
Hart, S.R., Dunn, T., 1993. Experimental cpx/melt partitioning of 24 trace elements. Contrib. Miner. Petrol. 113, 1–8. https://doi.org/10.1007/BF00320827.
Hess, H.H., 1960. Stillwater igneous complex. Geol. Soc. Am. Mem. 80, 1–230. https://doi.org/10.1130/MEM80-p1.
Hort, M., Marsh, B., Spohn, T., 1993. Igneous layering through oscillatory nucleation and crystal settling in well-mixed magmas. Contrib. Miner. Petrol. 114, 425–440. https://doi.org/10.1007/BF00321748.
Huppert, H.E., Sparks, R.S.J., 1984. Double-diffusive convection due to crystallization in magmas. An. Rev. Earth. Planet. Sci. 12, 11–37. https://doi.org/10.1146/annurev.ea.12.050184.000303.
Holness, M.B., Vukmanovic, Z., Mariani, E., 2017. Assessing the Role of Compaction in the Formation of Adcumulates: a Microstructural Perspective. J. Petrol. 58, 643–673. https://doi.org/10.1093/petrology/egx037.
Hosford, A., Tivey, M., Matsumoto, T., Dick, H., Schouten, H., Kinoshita, H., 2003. Crustal magnetization and accretion at the Southwest Indian Ridge near the Atlantis II Fracture Zone, 0–25 Ma. J. Geophys. Res.: Solid Earth 108. https://doi.org/10.1029/2001JB000604.
Ichiyama, Y., Morishita, T., Tamura, A., Arai, S., 2013. Petrology of peridotite xenolith bearing basaltic to andesitic lavas from the Shiribeshi Seamount, off northwestern Hokkaido, the Sea of Japan. J. Asian Earth Sci. 76, 48–58. https://doi.org/10.1016/j.jseaes.2013.07.031.
Jian, H., Singh, S.C., Chen, Y.J., Li, J., 2017a. Evidence of an axial magma chamber beneath the ultraslow-spreading Southwest Indian Ridge. Geology 45, 143–146. https://doi.org/10.1130/G38356.1.
Jian, H., Chen, Y.J., Singh, S.C., Li, J., Zhao, M., Ruan, A., Qiu, X., 2017b. Seismic structure and magmatic construction of crust at the ultraslow-spreading Southwest Indian Ridge at 50°28'E. J. Geophys. Res.: Solid Earth 122, 18–42. https://doi.org/10.1002/2016JB013377.
Jochum, K.P., Nohl, U., 2008. Reference materials in geochemistry and environmental research and the GeoReM database. Chem. Geol. 253, 50–53. https://doi.org/10.1016/j.chemgeo.2008.04.002.
Kimura, J.I., Ariskin, A.A., 2014. Calculation of water-bearing primary basalt and estimation of source mantle conditions beneath arcs: PRIMACALC2 model for WINDOWS. Geochem. Geophys. Geosyst. 15, 1494–1514. https://doi.org/10.1002/2014GC005329.
Kirkpatrick, R.J., 1975. Crystal growth from the melt: a review. Am. Mineral. 60, 798–814.
Kirkpatrick, R.J., Robinson, G.R., Hays, J.F., 1976. Kinetics of crystal growth from silicate melts: anorthite and diopside. J. Geophys. Res. [Atmos.] 81, 5715–5720. https://doi.org/10.1029/JB081i032p05715.
Kirkpatrick, R.J., 1977. Nucleation and growth of plagioclase, Makaopuhi and Alae lava lakes, Kilauea Volcano, Hawaii. Geol. Soc. Am. Bull. 88, 78–84. https://doi.org/10.1130/0016-7606(1977)88%3C78:NAGOPM%3E2.0.CO;2.
Koepke, J., Botcharnikov, R.E., Natland, J.H., 2018. Crystallization of late-stage MORB under varying water activities and redox conditions: Implications for the formation of highly evolved lavas and oxide gabbro in the ocean crust. Lithos 323, 58–77. https://doi.org/10.1016/j.lithos.2018.10.001.
Kogarko, L.N., Khapaev, V.V., 1987. The modeling of formation of apatite deposits of the Khibina massif (Kola Peninsula). In: Reidel, D. (Ed.), Parsons D (Edd) Origins of igneous layering. Dodrecht, pp. 589–611.
Lissenberg, C.J., Dick, H.J.B., 2008. Melt–rock reaction in the lower oceanic crust and its implications for the genesis of mid-ocean ridge basalt. Earth Planet. Sci. Lett. 271, 311–325. https://doi.org/10.1016/j.epsl.2008.04.023.
Lissenberg, C.J., MacLeod, C.J., Howard, K.A., Godard, M., 2013. Pervasive reactive melt migration through fast-spreading lower oceanic crust (Hess Deep, equatorial Pacific Ocean). Earth Planet. Sci. Lett. 361, 436–447. https://doi.org/10.1016/j.epsl.2012.11.012.
Lissenberg, C.J., MacLeod, C.J., 2016. A reactive porous flow control on mid-ocean ridge magmatic evolution. J. Petrol. 57, 2195–2220. https://doi.org/10.1093/petrology/egw074.
Longerich, H.P., Jackson, S.E., Gunther, D., 1996. Laser ablation inductively coupled plasma mass spectrometric transient signal data acquisition and analyte concentration calculation. J. Anal. At. Spectrom. 11, 899–904. https://doi.org/10.1039/JA9961100899.
MacLeod, C.J., Dick, H.J.B., Blum, P., Abe, N., Blackman, D.K., Bowles, J.A., Cheadle, M. J., Cho, K., Ciazela, J., Deans, J.R., Edgcomb, V.P., Ferrando, C., France, L., Ghosh, B., Ildefonse, B., John, B., Kendrick, M.A., Koepke, J., Leong, J.A.M., Liu, C., Ma, Q., Morishita, T., Morris, A., Natland, J.H., Nozaka, T., Plumper, O., Sanfilippo, A., Sylvan, J.B., Tivey, M.A., Tribuzio, R., Viegas, G., 2017. Site U1473. In: Proceedings of the International Discovery Program. IODP, College Station, TX, p. 360. https://doi.org/10.14379/iodp.proc.360.102.2017.
MacLeod, C.J., Dick, H.J.B., Allerton, S., Robinson, P.T., Coogan, L.A., Edwards, S.J., Galley, A., Gillis, K.M., Hirth, G., Hunter, A.G., Hutchinson, D., 1998. Geological mapping of slow-spread lower ocean crust: a deep-towed video and wireline rock drilling survey of Atlantis Bank (ODP Site 735, SW Indian Ridge). InterRidge News 7, 39–43.
MacLeod, C.J., Searle, R.C., Murton, B.J., Casey, J.F., Mallows, C., Unsworth, S.C., Achenbach, K.L., Harris, M., 2009. Life cycle of oceanic core complexes. Earth Planet. Sci. Lett. 287, 333–344. https://doi.org/10.1016/j.epsl.2009.08.016.
Magde, L.S., Barclay, A.H., Toomey, D.R., Detrick, R.S., Collins, J.A., 2000. Crustal magma plumbing within a segment of the Mid-Atlantic Ridge, 35°N. Earth Planet. Sci. Lett. 175, 55–67. https://doi.org/10.1016/S0012-821X(99)00281-2.
McBirney, A.R., Noyes, R.M., 1979. Crystallization and layering of the Skaergaard intrusion. J. Petrol. 20, 487–554. https://doi.org/10.1093/petrology/20.3.487.

McDonough, W.F., Sun, S.S., 1995. The composition of the Earth. Chem. Geol. 120, 223–253. https://doi.org/10.1016/0009-2541(94)00140-4.
Meurer, W.P., Boudreau, A.E., 1998. Compaction of igneous cumulates Part II: Compaction and the development of igneous foliations. J. Geol. 106, 293–304. https://doi.org/10.1086/516023.
Meyer, P.S., Dick, H.J.B., Thompson, G., 1989. Cumulate gabbros from the Southwest Indian Ridge, 54° S-7° 16′ E: Implications for magmatic processes at a slow spreading ridge. Contrib. Miner. Petrol. 103, 44–63. https://doi.org/10.1007/BF00371364.
Meyzen, C.M., Toplis, M.J., Humler, E., Ludden, J.N., Mével, C., 2003. A discontinuity in mantle composition beneath the southwest Indian ridge. Nature 421, 731–733. https://doi.org/10.1038/nature01424.
Mollo, S., Hammer, J.E., 2017. Dynamic crystallization in magmas. In: Heinrich W, Abart R (Eds), Mineral reaction kinetics: Microstructures, textures, chemical and isotopic signatures, EMU Notes in Mineralogy 16, 373–418. https://doi.org/10.1180/EMUnotes.16.12.
Morishita, T., Ishida, Y., Arai, S., Shirasaka, M., 2005. Determination of multiple trace element compositions in thin (< 30 μm) layers of NIST SRM 614 and 616 using laser ablation inductively coupled plasma-mass spectrometry. Geostand. Geoanal. Res. 29, 107–122. https://doi.org/10.1111/j.1751-908X.2005.tb00659.x.
Mutter, J.C., Karson, J.A., 1992. Structural processes at slow-spreading ridges. Science 257, 627–634. https://doi.org/10.1126/science.257.5070.627.
Natland, J.H., Meyerr, P.S., Dick, H.J.B., Bloomer, S.H., 1991. Magmatic oxides and sulfides in gabbroic rocks from hole 735B and the later development of the liquid line of descent. In: Von Herzen, R.P., Robinson, P.T., et al., Proceedings of the Ocean Drilling Program, Scientific Results, 118. College Station, TX (Ocean Drilling Program), pp. 75-111. 10.2973/odp.proc.sr. 118.163.1991.
Natland, J.H., Dick, H.J.B., 2001. Formation of the lower ocean crust and the crystallization of gabbroic cumulates at a very slowly spreading ridge. J. Volcanol. Geoth. Res. 110, 191–233. https://doi.org/10.1016/S0377-0273(01)00211-6.
Natland, J.H., Dick, H.J.B., Miller, D.J., Von Herzen, R.P. (Eds.), 2002. In: Proc. ODP, Sci. Results, 176: College Station, TX (Ocean Drilling Program). doi:10.2973/odp.proc.sr.176.2002.
Natland, J.H., Dick, H.J.B., 2002. Stratigraphy and composition of gabbros drilled in Ocean Drilling Program Hole 735B, Southwest Indian Ridge: a synthesis of geochemical data. In: Natland, J.H., Dick, H.J.B., Miller, D.J., Von Herzen, R.P. (Eds.), Proceedings of the Ocean Drilling Program, Scientific Result, 176. College Station, TX (Ocean Drilling Program), 1-69. doi:10.2973/odp.proc.sr.176.002.2002.
Naslund, H.R., McBirney, A.R., 1996. Mechanisms of formation of igneous layering. In: Cawthorn RG (Eds), Layered intrusions. Elsevier, Amsterdam, pp 1–43. https://doi.org/10.1016/S0167-2894(96)80003-0.
Nguyen, D.K., Morishita, T., Soda, Y., Tamura, A., Ghosh, B., Harigane, Y., France, L., Liu, C., Natland, J.H., Sanfilippo, A., MacLeod, C.J., Blum, P., Dick, H.J.B., 2018. Occurrence of Felsic Rocks in Oceanic Gabbros from IODP Hole U1473A: Implications for Evolved Melt Migration in the Lower Oceanic Crust. Minerals 8, 583. https://doi.org/10.3390/min8120583.
Nisbet, E.G., Fowler, C.M.R., 1978. The Mid-Atlantic Ridge at 37 and 45°N: some geophysical and petrological constraints. Geophys. J. Int. 54, 631–660. https://doi.org/10.1111/j.1365-246X.1978.tb05499.x.
Niu, Y., 1997. Mantle melting and melt extraction processes beneath ocean ridges: evidence from abyssal peridotites. J. Petrol. 38, 1047–1074. https://doi.org/10.1093/petroj/38.8.1047.
Niu, Y., Hékinian, R., 1997. Spreading rate dependence of the extent of mantle melting beneath ocean ridges. Nature 385, 326–329. https://doi.org/10.1038/385326a0.
Niu, Y., Gilmore, T., Mackie, S., Greig, A., Bach, W., 2002. Mineral chemistry, whole-rock compositions, and petrogenesis of Leg 176 gabbros: data and discussion. In: Natland, J.H., Dick H.J.B., Miller, D.J., Von Herzen, R.P. (Eds.), Proceedings of the Ocean Drilling Program, Scientific Results, 176. College Station, TX, pp. 1-60. doi:10.2973/odp.proc.sr.176.011.2002.
Niu, Y., Langmuir, C.H., Kinzler, R.J., 1997. Origin of abyssal peridotites: a new perspective. Earth Planet. Sci. Lett. 52, 251–265. https://doi.org/10.1016/S0012-821X(97)00119-2.
Olive, J.A., Behn, M.D., Tucholke, B.E., 2010. The structure of oceanic core complexes controlled by the depth distribution of magma emplacement. Nat. Geosci. 3, 491–495. https://doi.org/10.1038/ngeo888.
Pearce, N.J.G., Perkins, W.T., Westgate, J.A., Gorton, M.P., Jackson, S.E., Neal, C.R., Chenery, S.P., 1997. A compilation of new and published major and trace element data for NIST SRM 610 and NIST SRM 612 glass reference materials. Geostandard Newslett. 21, 115–144. https://doi.org/10.1111/j.1751-908X.1997.tb00538.x.
Perfit, M.R., Chadwick, W.W., 1998. Magmatism at mid-ocean ridges: Constraints from volcanological and geochemical investigations. In: Buck, W.R., Delaney, P. T., Karson, J.A., Lagabrielle, Y. (Eds.), Faulting and Magmatism at Mid-Ocean Ridges: Geophys. Monogr. Ser., 106. AGU, pp. 59-116. https://doi.org/10.1029/GM106p0059.
Pettigrew, T.J., Casey, J.F., Miller, D.J., Araki, E., Boissonnas, R., Busby, R., Einaudi, F., Gerdom, M., Guo, Z.P., Hopkins, H., Myers, G., 1999. Proceedings of the Ocean Drilling Program, Initial Reports. TX (Ocean Drilling Program), College Station, p. 179.
Ridley, W.I., Perfit, M.R., Smith, M.C., Fornari, D.J., 2006. Magmatic processes in developing oceanic crust revealed in a cumulate xenolith collected at the East Pacific Rise, 9°50′ N. Geochem. Geophys. Geosyst. 7. https://doi.org/10.1029/2006GC001316.
Sanfilippo, A., Dick, H.J.B., Marschall, H.R., Lissenberg, C.J., Urann, B., 2019. Emplacement and high-temperature evolution of gabbros of the 16.5°N oceanic core complexes (Mid-Atlantic Ridge): Insights into the compositional variability of the lower oceanic crust. Geochem. Geophys. Geosyst. 20, 46–66. https://doi.org/10.1029/2018GC007512.
Sanfilippo, A., MacLeod, C.J., Tribuzio, R., Lissenberg, C.J., Zanetti, A., 2020. Early-Stage Melt-Rock Reaction in a Cooling Crystal Mush Beneath a Slow-Spreading Mid-Ocean Ridge (IODP Hole U1473A, Atlantis Bank, Southwest Indian Ridge). Front. Earth Sci. 8, 473. https://doi.org/10.3389/feart.2020.579138.
Sanfilippo, A., Tribuzio, R., Tiepolo, M., Berno, D., 2015. Reactive flow as dominant evolution process in the lowermost oceanic crust: evidence from olivine of the Pineto ophiolite (Corsica). Contrib. Miner. Petrol. 170. https://doi.org/10.1007/s00410-015-1194-8.
Saper, L., Liang, Y., 2014. Formation of plagioclase-bearing peridotite and plagioclase bearing wehrlite and gabbro suite through reactive crystallization: an experimental study. Contrib. Miner. Petrol. 167, 1–16. https://doi.org/10.1007/s00410-014-0985-7.
Sauter, D., Cannat, M., Rouméjon, S., Andreani, M., Birot, D., Bronner, A., Brunelli, D., Carlut, J., Delacour, A., Guyader, V., MacLeod, C.J., 2013. Continuous exhumation of mantle-derived rocks at the Southwest Indian Ridge for 11 million years. Nat. Geosci. 6, 314–320. https://doi.org/10.1038/ngeo1771.
Singh, S.C., Crawford, W.C., Carton, H., Seher, T., Combier, V., Cannat, M., Pablo Canales, J., Düsünür, D., Escartin, J., Miguel Miranda, J., 2006. Discovery of a magma chamber and faults beneath a Mid-Atlantic Ridge hydrothermal field. Nature 442, 1029–1032. https://doi.org/10.1038/nature05105.
Sinha, M.C., Navin, D.A., MacGregor, L.M., Constable, S., Peirce, C., White, A., Heinson, G., Inglis, M.A., 1997. Evidence for accumulated melt beneath the slow–spreading Mid– Atlantic Ridge. Philos. Trans. R. Soc. London, Ser. A: Mathematical Physical and Engineering Sciences 355, 233–253. https://doi.org/10.1098/rsta.1997.0008.
Sinha, M.C., Constable, S.C., Peirce, C., White, A., Heinson, G., MacGregor, L.M., Navin, D.A., 1998. Magmatic processes at slow spreading ridges: Implications of the RAMESSES experiment at 57°45′ N on the Mid-Atlantic Ridge. Geophys. J. Int. 135, 731–745. https://doi.org/10.1046/j.1365-246X.1998.00704.x.
Sinton, J.M., Detrick, R.S., 1992. Mid-ocean ridge magma chambers. J. Geophys. Res.: Solid. Earth 97, 197–216. https://doi.org/10.1029/91JB02508.
Smith, P.M., Asimow, P.D., 2005. Adiabat_1ph: A new public front-end to the MELTS, pMELTS, and pHMELTS models. Geochem. Geophys. Geosyst. 6. https://doi.org/10.1029/2004GC000816.
Sun, S.S., McDonough, W.F., 1989. Chemical and isotopic systematics of oceanic basalts: implications for mantle composition and processes. J. Geol. Soc. London Spec. Publ. 42, 313–345. https://doi.org/10.1144/GSL.SP.1989.042.01.19.
Tamura, A., Akizawa, N., Otsuka, R., Kanayama, K., Python, M., Morishita, T., Arai, S., 2015. Measurement of whole-rock trace-element composition by flux-free fused glass and LA-ICP-MS: evaluation of simple and rapid routine work. Geochem. J. 49, 243–258. https://doi.org/10.2343/geochemj.2.0353.
Tribuzio, R., Manatschal, G., Renna, M.R., Ottolini, L., Zanetti, A., 2020. Tectono-magmatic interplay and related metasomatism in gabbros from the Chenaillet ophiolite (Western Alps). J. Petrol. 60, 2483–2508. https://doi.org/10.1093/petrology/egaa015.
Tucholke, B.E., Behn, M.D., Buck, W.R., Lin, J., 2008. Role of melt supply in oceanic detachment faulting and formation of megamullions. Geology 36, 455–458. https://doi.org/10.1130/G24639A.1.
Van Ark, E.M., Detrick, R.S., Canales, J.P., Carbotte, S.M., Harding, A.J., Kent, G.M., Nedimovic, M.R., Wilcock, W.S.D., Diebold, J.B., Babcock, J.M., 2007. Seismic structure of the Endeavour Segment, Juan de Fuca Ridge: Correlations with seismicity and hydrothermal activity. J. Geophys. Res.: Solid Earth, 112. https://doi.org/10.1029/2005JB004210.
Van den Bleeken, G., Müntener, O., Ulmer, P., 2011. Melt variability in percolated peridotite: An experimental study applied to reactive migration of tholeiitic basalt in the upper mantle. Contrib. Miner. Petrol. 161, 921–945. https://doi.org/10.1007/s00410-010-0572-5.
White, W.M., Klein, E.M., 2014. Composition of the oceanic crust. In: Holland, H.D., Turekian, K.K. (Eds.), Treatise on Geochemistry, 4. Elsevier, pp. 457-496. http://dx.doi.org/10.1016/B0-08-043751-6/03016-4.
Zhang, W., Liu, C., Dick, H.J.B., 2020. Evidence for Multi-stage Melt Transport in the Lower Ocean Crust: Atlantis Bank Gabbroic Massif (IODP Hole U1473A, SW Indian Ridge). J. Petrol. 61. https://doi.org/10.1093/petrology/egaa082.